

Imaging the heart of astrophysical objects with optical long-baseline interferometry

J.-P. Berger^{1,2} · F. Malbet¹ · F. Baron^{3,4} ·
A. Chiavassa^{5,19} · G. Duvert^{1,6} · M. Elitzur⁷ ·
B. Freytag⁸ · F. Gueth⁹ · S. Hönl^{10,11} · J. Hron¹² ·
H. Jang-Condell¹³ · J.-B. Le Bouquin^{2,1} ·
J.-L. Monin¹ · J.D. Monnier³ · G. Perrin¹⁴ ·
B. Plez¹⁵ · T. Ratzka¹⁶ · S. Renard¹ · S. Steff² ·
E. Thiébaud⁸ · K. Tristram¹⁰ · T. Verhoelst¹⁷ ·
S. Wolf¹⁸ · J. Young⁴

Received: date / Accepted: date

Abstract The number of publications of aperture-synthesis images based on optical long-baseline interferometry measurements has recently increased due to easier access to visible and infrared interferometers. The interferometry technique has now reached a technical maturity level that opens new avenues for numerous astrophysical topics requiring milli-arcsecond model-independent imaging. In writing this paper our motivation was twofold: 1) review and publicize emblematic excerpts of the impressive corpus accumulated in the field of optical interferometry image reconstruction; 2) discuss future prospects for this technique by selecting four representative astrophysical science cases in order to review the potential benefits of using optical long baseline interferometers.

For this second goal we have simulated interferometric data from those selected astrophysical environments and used state-of-the-art codes to provide the reconstructed images that are reachable with current or soon-to-be facilities. The image reconstruction process was “blind” in the sense that reconstructors had no knowledge of the input brightness distributions. We discuss the impact of optical interferometry in those four astrophysical fields. We show that image reconstruction software successfully provides accurate morphological information on a variety of astrophysical topics and review the current strengths and weaknesses of such reconstructions.

1: Université J. Fourier (Grenoble 1)/CNRS, UMR 5571, Institut de Planétologie et d’Astrophysique de Grenoble, B.P. 53, F-38041 Grenoble cedex 9, France · **2:** European Southern Observatory, Santiago, Chile · **3:** University of Michigan, Ann Arbor, USA · **4:** Cavendish Laboratory, University of Cambridge, Cambridge, United Kingdom · **5:** Max-Planck-Institut für Astrophysik, Garching bei München, Germany · **6:** Jean Marie Mariotti Center, Grenoble, France · **7:** University of Kentucky, Lexington, USA · **8:** Centre de Recherche en Astrophysique de Lyon, UMR 5574 Université de Lyon/École Normale Supérieure de Lyon/CNRS, Lyon, France · **9:** Institut de Radioastronomie Millimétrique, Grenoble, France · **10:** Max-Planck-Institut für Radioastronomie, Bonn, Germany · **11:** University of California in Santa Barbara, Department of Physics, Santa Barbara, USA · **12:** Institut für Astronomie, Universität Wien, Wien, Austria · **13:** Department of Physics & Astronomy 1000 E. University of Wyoming 3905 Laramie, WY, 82071 · **14:** Laboratoire d’Etudes Spatiales et d’Instrumentation en Astrophysique, UMR 8109 Observatoire de Paris/CNRS, Meudon, France · **15:** Laboratoire Univers et Particules de Montpellier, UMR 5299, CNRS, Université Montpellier 2, 34095 Montpellier, France · **16:** Universitäts-Sternwarte München, München, Germany · **17:** Institute of Astronomy, KULeuven, Belgium · **18:** University of Kiel, Kiel, Germany · **19:** Institut d’Astronomie et d’Astrophysique, Université Libre de Bruxelles, Bruxelles, Belgium

We investigate how to improve image reconstruction and the quality of the image possibly by upgrading the current facilities. We finally argue that optical interferometers and their corresponding instrumentation, existing or to come, with 6 to 10 telescopes, should be well suited to provide images of complex sceneries.

Keywords Instrumentation: interferometers · Techniques: interferometric · Methods: data processing · planetary systems: protoplanetary disks · stars: supergiants · stars: AGB - circumstellar matter · stars: imaging · Galaxies: active · Galaxies nuclei

1 Introduction

The recent years have seen a significant increase in scientific publications making use of images based on homodyne optical long-baseline interferometry (e.g. Monnier et al, 2007; Le Bouquin et al, 2009; Schmitt et al, 2009; Lacour et al, 2009; Kraus et al, 2009; Haubois et al, 2009; Kloppenborg et al, 2010; Millour et al, 2011). While model fitting of visibilities remains today the most accurate way to characterize an object brightness distribution, the technique has now reached a technical maturity level that opens new avenues for numerous astrophysical topics requiring milli-arcsecond model-independent imaging.

These results are the culmination of years of efforts that started with speckle interferometry, aperture masking and long-baseline interferometry. For the latter active or defunct prototype facilities such as COAST, IOTA, I2T, GI2T, Mark III, NPOI, PTI, SUSI¹, have progressively paved the way for large diameter telescope arrays such as CHARA, Keck Interferometer, and VLTI.

In order to assess the main astrophysical questions that visible and infrared interferometry can actually answer, we first review the status of optical interferometry in terms of image synthesis achievements and then follow up with a discussion on the important issues from four main astrophysical fields namely planetary formation, stellar atmospheres, circumstellar shells, and active galactic nuclei². Then, we simulate interferometric data from those environments and provide the reconstructed images that are achievable with current or near-future facilities, in order to discuss the impact of such techniques in those fields.

The paper is organized as follows. The principle of interferometric imaging as well as a brief description of present imaging interferometers is given in Sect. 2. The four astrophysical topics are briefly described in Section 3 and for each one the parameters of the simulations are presented. The imaging facilities are reviewed in Section 4. In Sect. 5 we describe the process which allows us to produce realistic interferometric data and then reconstructed images. Finally, Section 6 is devoted to a discussion of the results and the future perspectives for optical long-baseline interferometry.

2 Imaging with a long baseline interferometer

2.1 Principles of optical long baseline interferometry

Principles of long baseline interferometry are well explained in numerous articles, conference proceedings and monographies. The reader is referred to Thompson et al (2001) for a

¹ ISI belongs to the same fraternity but operates in heterodyne mode and will therefore not be discussed.

² This choice, obviously not exhaustive, should not hide the wealth of astronomical topics requesting milli-arcsecond resolution imaging: Cepheids, magnetic, Be, O, supermassive stars, stellar mass loss, jet formation, dynamics of close stellar clusters, SMBH galaxies etc.

detailed description of the technique which lays out nicely most of the fundamental principles, albeit mostly oriented towards radio astronomy. More recently there have been interesting collective works, review articles and monographies dedicated to the specifics of optical long baseline interferometry (e.g. Lawson, 2000; Monnier, 2003; Haniff, 2007; Malbet and Perrin, 2007; Glindemann, 2011). In our definition, optical interferometry covers the wavelength regime from the visible $0.4\mu\text{m}$ to the mid infrared $10 - 20\mu\text{m}$.

An interferometric array measures the spatio-temporal coherence of the electromagnetic field through two or more telescopes (e.g. Goodman, 1985). The core observable of an interferometer is the complex visibility V_{kl} :

$$V_{kl} = |V_{kl}| \exp^{j\Phi_{kl}} \quad (1)$$

Where $|V_{kl}|$ is the amplitude of the visibility and Φ_{kl} its phase. V_{kl} is extracted from the measurement of the contrast and phase of the interferogram formed between two telescopes k and l . Unlike radio interferometers, where the detection of the electromagnetic field is done at the telescope level (heterodyne interferometry), most optical interferometers require the actual formation of interferometric fringes on a detector.

The fundamental theorem of long baseline interferometry is the Van-Cittert Zernike theorem (Goodman, 1985; Thompson et al, 2001). It relates the complex visibility V measured at a spatial frequency \mathbf{B}/λ (\mathbf{B} being the telescope baseline vector and λ the wavelength) to the actual object brightness $I(\mathbf{x})$ distribution through a Fourier transform relation.

$$V(\mathbf{B}/\lambda) = \frac{\int_{-\infty}^{\infty} I(\mathbf{x}) \exp^{-2\pi j\mathbf{x}\mathbf{B}/\lambda} d\mathbf{x}}{\int_{-\infty}^{\infty} I(\mathbf{x}) d\mathbf{x}} \quad (2)$$

The components (u, v) of \mathbf{B}/λ form the spatial frequency coordinate system. \mathbf{x} represents the angular position vector. Therefore, interferometric observations provide information about spatial frequency components of the brightness distribution. Similarly to the ‘‘Rayleigh criterion’’ used in single pupil telescopes, one can define the resolution of a two-telescope interferometer of baseline B as $\lambda/2B$ (in radians) which corresponds approximately to the milli-arcsecond level in the near infrared with typical hectometric baselines. The amplitude of the visibility is related to the projected brightness angular size while the phase provides information on the brightness photocenter location.

In practice, visible and infrared interferometry require mixing the light received from an astronomical source and collected by several independent telescopes separated from each other by tens or even hundreds of meters³. The light beams are then overlapped and form an interference pattern if the optical path difference between the different arms of the interferometer —taking into account paths from the source up to the detector— is smaller than the coherence length of the incident wave (typically of the order of several microns). This interference pattern is composed of fringes, i.e. a succession of stripes of faint (destructive interferences) and bright (constructive interferences) intensity. By measuring (i) the contrast of these fringes, i.e. the normalized flux difference between the maximum and minimum intensity, also called the visibility amplitude, and (ii) their phase, i.e. their position, one can construct an estimation of the so-called complex visibility.

³ With the notable exception of the heterodyne ISI interferometer (Townes and Wishnow, 2008)

2.2 Obstacles to imaging with an optical interferometer

In principle, measuring the complex visibilities at all spatial frequencies up to a maximum value $u\mathbf{v}_{\max}$, should permit the retrieval of the synthesized image of the spatial intensity distribution of the object with a spatial resolution $1/u\mathbf{v}_{\max}$ by inverse Fourier transforming the 2-D visibility map. However there are two main obstacles to this simple inversion.

First, in all practical cases, the (u, v) plane cannot be fully covered, because the spatial frequencies sampled by an interferometer are limited by the number of pairs of telescopes. With the Earth rotation these spatial frequencies follow (u, v) tracks in shape of arcs of ellipses (Thompson et al, 2001; Ségransan, 2007) which provides *super-synthesis* (also called “Earth rotation synthesis”) and therefore increases the coverage. In the particular cases where no strong wavelength dependence of the object brightness distribution is expected, one can use measurements at different wavelengths to help further extend the (u, v) coverage, but only radially.

Secondly, the phases of the visibilities are frequently lost because they have been scrambled by atmospheric blurring effects (Quirrenbach, 2000). Instrumental effects also contribute but in a more static way. In the optical domain (as in the radio but on a wilder scale), rapid fluctuations in the atmospheric optical index induce random optical path variations. Typical atmospheric coherence times at these wavelengths are in the range of 1 to 10 milliseconds. Consequently, measuring direct phase information is challenging. Several techniques have been explored to circumvent this difficulty, all of which have inherited from experience in radio interferometry, and are well detailed in Monnier (2007).

- The phase of the product of the 3 complex visibilities measured with 3 telescopes forming a closed triangle, called the closure phase, was first introduced by Jennison (1958) in order to cancel out instrumental and atmosphere-induced phase errors and recover partial phase information. It was later pioneered in the optical domain by Baldwin et al (1986) and subsequent aperture masking experiments at Cambridge and is now a routine observable of optical interferometers. Parallel to that, triple-correlation techniques used in speckle interferometry (e.g Weigelt, 1991) also make use of closure phase although the formal relation between the two techniques was established by Roddier (1986). In practice, the closure phase is estimated from the phase of the so-called “bi-spectrum” B_{ijk} which is constructed from the product of complex visibilities estimated in a closed triangle $B_{ijk} = V_{ij} V_{jk} V_{ki}$.
- The *self-calibration* method as described by Cornwell and Wilkinson (1981) aims at retrieving phase information on a maximum number of baselines from closure phase estimators. It integrates the phase recovery procedure in the image reconstruction process. For that purpose it uses an iterative scheme that starts from a trial image and seeks, through modeling and fitting of atmospheric and telescope phase errors, to find the best phase estimation consistent with closure phases.
- *Phase referencing* encompasses various techniques that aim at measuring, as directly as possible, the phases. The idea is to calibrate the phase measurement with a phase reference, either internal or external. *Differential phases*, which are obtained by comparing phases at different wavelengths with a reference channel, provide direct means of phase estimation. This is true provided one can constrain the morphology at the reference wavelength (e.g an unresolved emission in a continuum channel) and model the atmospheric and instrumental differential phase. The reader is referred to the work of Vakili et al (1997), for example, for illustration of the differential phase extraction, and Schmitt et al (2009) and previous NPOI team publications for a detailed demonstration

of spectral differential imaging. *Astrometric phase referencing* uses the capability of observing two objects within the atmospheric isoplanatic patch to provide an astrometric reference to the phase (with the motivation of authorizing longer integration times if a nearby bright source can be used as a reference). This requires a specific infrastructure allowing for dual-star observation. It has been implemented at PTI, NPOI, and is being implemented at Keck and VLTI (e.g. Delplancke, 2008) but has not led yet to notable mapping results.

2.3 Principles of image reconstruction

Because of the voids in the (u, v) plane coverage and the lack of complete phase information, a given set of data can be fitted by several different brightness distributions. The image power spectra and bispectra of all these distributions fit the data within the error bars in the least squared sense. Hence, additional prior information is required to discriminate between those images and to further constrain the solutions. The best image is defined as the most probable image given the data and prior information. The bias toward the prior is the price to pay to select an image from such sparse data. Reconstructing an image consists then in minimizing a quantity connected to the data and to the prior with respect to the pixel values of the image (Thiebaut and Giovannelli, 2010):

$$\mathbf{x}_{\text{best}} = \operatorname{argmin}_{\mathbf{x} \in \Omega} [f_{\text{data}}(\mathbf{x}; \mathbf{y}) + \mu f_{\text{prior}}(\mathbf{x})] \quad (3)$$

where \mathbf{x} are the image parameters (e.g. the *pixel* values) constrained to belong to the feasible set Ω of, e.g., non-negative and normalized images, f_{data} measures the discrepancy between the image model and the data \mathbf{y} , f_{prior} is the *regularization* term which enforces the priors and the hyperparameter μ is a weight factor that tunes the balance between these two terms.

The term f_{data} is usually derived from an analytical model of the data and the statistics of the noise, although slightly different approximations (e.g., Meimon et al, 2005) are made by current image synthesis algorithms. Note that f_{data} may be itself the sum of different terms to account for different kinds of data such as power spectra and phase closures.

The term f_{prior} is used to inject in the minimization process a priori knowledge on the object. In addition to fundamental constraints such as positivity (i.e. intensity can not be negative) and limited field of view there are numerous possible priors that can be included in the regularization. Although automation of the image reconstruction process is highly desirable, most of current (u, v) coverages in optical interferometry leave room for multiple possible solutions. Therefore the observer cannot avoid introducing, through the regularization, his knowledge of the expected brightness distribution. The interested reader is referred to the recent work by Renard et al (2011) for a benchmarking of regularizations.

There are several popular regularizations.

1. Maximum Entropy Method (MEM, Gull and Skilling, 1984; Skilling and Bryan, 1984a; Narayan and Nityananda, 1986). This is one of the most employed techniques. It tries to find the smoothest image compatible with the data while keeping high frequency information. For that purpose it uses a smoothness scalar estimator called *entropy* which has several possible definitions, one of the most popular being the Gull-Skilling entropy (Skilling and Bryan, 1984b). MEM will find the image that best fits the data and keeps entropy maximum. Because of the smoothness requirements MEM will introduce *super-resolution* to the image, i.e. it will put information at spatial frequencies higher than the usual optical Rayleigh criterion.

2. *Compactness* allows the definition of a spatial zone outside of which no flux is expected.
3. *Total Variation* tries to minimize the total gradient of the image. It favors parts of the image with uniform zones and fast intensity changes (like a stellar surface). It has been found by Renard et al (2011) as one the best “all-terrain” regularization methods when applied to different object morphologies.
4. *Smoothness* regularization smooths the image but can be adjusted to preserve some sharp variations at edges or point-like structures, favor some regions in the image etc. There are various ways to force and control smoothness.
5. *Sparseness* aims at restoring an image with the smallest number of components (*e.g.* CLEAN method in radio-astronomy or Building Block Method in optical interferometry, see below).

Figure 1 illustrates visually the effect of different prior regularizations on different types of brightness distributions. The first column is a doughnut like structure surrounding a central star. The middle column is a photosphere with limb-darkening. The last column is a galaxy composed of extended and point-like emission. The prior regularizations, from top to bottom, are: the original image, smoothness, compactness, total variation, smoothness with sharp boundaries (*e.g.* $\ell_2 - \ell_1$ norm), ℓ_p norm with $p = 0.5$ and $p = 2$, squared-root MEM and MEM with gaussian a priori image.

2.4 Imaging algorithms and their application

In the radio domain the CLEAN algorithm (Högbom, 1974) and its different flavors associated or not with self-calibration (Cornwell and Wilkinson, 1981) have been the dominant tools for image reconstruction. This is not the case in optical long baseline interferometry where mapping techniques are still the subject of active research. It is essentially the absence of direct phase information that has triggered new developments with respect to radio-astronomy. Although this effort started with the rise of aperture masking (Baldwin et al, 1986; Haniff et al, 1987; Readhead et al, 1988) in single-dish telescopes, the similarities are so strong that both techniques can use the same tools. For our purposes we can safely ignore the specificities. Here we discuss the methods that are being actively used in actual astrophysical programs and are sometimes tailored to deal with different source structures and the number of telescopes used.

The Building Block Method (BBM) has been proposed by Hofmann and Weigelt (1993) and offers many similarities with the CLEAN method except that it can handle bispectra (and hence closure phases). The minimization is carried through a matching pursuit algorithm that imposes the sparsest solution.

The BiSpectrum Maximum Entropy Method (BSMEM) uses the MEM method to regularize the image reconstruction process using visibility amplitudes and bispectra. It supposes independent gaussian statistics for amplitude and closure phase and uses the Gull-Skilling (Skilling and Bryan, 1984b) entropy as regularization criterion. Image entropy provides a metric to measure smoothness in the image. This criterion will minimize the regularization weight based on the comparison with a reference image that can be updated through an iterative process. It uses a specific numerical optimizer MEMSYS that implements the strategy established by Skilling and Bryan (1984a) and can handle any type of data.

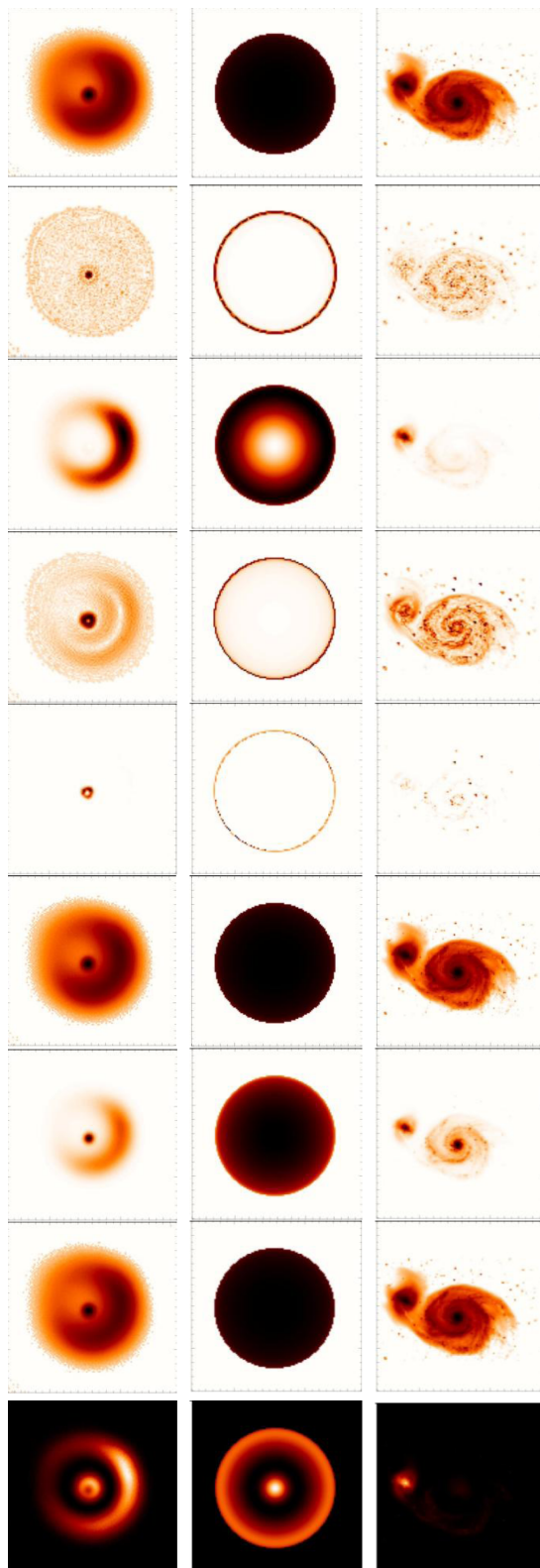


Fig. 1 Effects of different priors. From left to right: reconstructed images of a doughnut like structure surrounding a central star, a photosphere with limb-darkening and a galaxy composed of extended and point-like emission. From top to bottom: original image, smoothness, compactness, total variation, smoothness with sharp boundaries (e.g $\ell_2 - \ell_1$ norm), ℓ_p norm with $p = 0.5$ and $p = 2$, squared-root MEM and MEM with gaussian a priori image.

Table 1 Comparison of the image synthesis algorithms used in optical interferometry.

Code name	Data	Regularization	Optimization Strategy
MiRA	any	positivity, total variation, ℓ_2 , $\ell_2-\ell_1$, Gull-Skilling entropy with floating or given prior image	limited memory quasi-Newton with bound (positivity) and normalization constraints
BSMEM	bispectra, power spectra, complex visibilities	Gull-Skilling entropy with given prior image, multi-scale entropy	non-linear conjugate gradients with unsupervised hyper parameter control
WISARD	pseudo-complex visibilities formed from phase closures and power spectra	positivity, ℓ_2 , $\ell_2-\ell_1$	alternative minimization and self calibration
BBM	bispectra	positivity, sparseness	matching pursuit
MACIM	any	any	global optimization by simulated annealing

MEM and self-calibration Here, the maximum entropy method is embedded in an interactive process that starts with a guess on the instrument phases compliant with the closure phase measurements. The iteration includes fitting telescope atmospheric and instrumental phase errors and remapping of the image while respecting the closure phases. It therefore iterates in order to converge to the most probable image using the best guessed phases.

The MACIM algorithm (MARkov Chain Imager Ireland et al, 2006), unlike the preceding tries to find globally the images that are optimal in the Bayesian sense (and not the image that apparently fits best the data). For that purpose it tries to maximize the *a posteriori* probability:

$$\Pr(\mathbf{x}, \mathbf{y}) = \exp \left[-\frac{1}{2} (f_{\text{data}} + \mu f_{\text{prior}}) \right] \quad (4)$$

and therefore can provide a joint probability density of the probable images. It can use or not use regularizations (currently MEM and dark zone connectivity) and handles any kind of data.

The MIRA algorithm (Multi-aperture Image Reconstruction Algorithm, Thiébaud, 2008) minimizes Eq. (3) by using a non linear optimization algorithm. Because the method does not allow a global optimization, it will depend on using the initial image as a constraint. It does not try to reconstruct the phases directly and therefore can handle closure phases data and any other observable. It encodes many types of regularization which offers the possibility of testing the reliability of the reconstructed images.

The WISARD algorithm (Weak-phase Interferometric Sample Alternating Reconstruction Device, Meimon et al, 2008), is an application of the self-calibration idea to optical interferometry. It reconstructs the phases from the closure phases. The phase inversion process has multiple minima and therefore the global minimization is a multi-modal problem and can depend on the initial image.

Table 1 summarizes the features of the different algorithms that were specifically designed to cope with optical interferometry data. These algorithms are the main challengers

of the *Interferometric Imaging Beauty Contests* which, every two years since 2004, quantitatively compares the results of various image synthesis methods on simulated optical interferometric data (Lawson et al, 2004, 2006; Cotton et al, 2008; Malbet et al, 2010). Among these algorithms, BSMEM (Buscher, 1994; Baron and Young, 2008) and MiRA (Thiébaud, 2008) have repeatedly won the contest for data sets typical of next generation instruments. These are the ones that were used to produce the images from simulated data sets presented in this paper, together with MACIM (Ireland et al, 2006).

2.5 Examples

In this section, we describe some selected significant astrophysical publications making use of reconstructed imaging (Fig. 2). While we acknowledge that these choices suffer from selection effects, (for example we have limited the amount of binary images) we believe that these examples illustrate well the state of the art.

Image 1 in Fig. 2 shows one of the early attempts by Quirrenbach et al (1994) to reconstruct images out of visibility amplitude data using the Mark III interferometer. Even without phases they were able, using MEM-inspired methods, to map the H_α emission around ζ Tauri showing clearly its extension and flattening (related to its inclination). The absence of phases appears in the centro-symmetry of the image.

Images 2 and 3 in Fig. 2 show the pioneering images of binaries obtained at COAST (Baldwin et al, 1996) and NPOI (now NOI) (Benson et al, 1997) using standard radio packages associated with self-calibration (for the NOI reconstruction).

Young et al (2000) used aperture masking and the COAST to map the surface of Betelgeuse. In image 4, the aperture masking image obtained with the William Herschel Telescope is shown. The surface is marginally resolved since the angular resolution is barely sufficient. The image was obtained with the combination of the MEM method and self-calibration. More recently Haubois et al (2009) imaged the spotty surface of Betelgeuse using IOTA (images 5 and 6 of Fig. 2). Both WISARD and MIRA reconstructions lead to the same result confirming what had already revealed by Young et al (2000). In this case, both the dynamic range and the ability to characterize the spots are limited by the instrument accuracy and the difficulty for an interferometer to lock on low visibilities. This constraint has to be taken into account in the design of any future “imaging instrument”, as we will discuss later.

Images 7 to 9 of Fig. 2 are reconstructed images of respectively Altair, T Leporis and Epsilon Aurigae. Images 7 and 9 were obtained with CHARA using MACIM and BSMEM (respectively Monnier et al, 2007; Kloppenborg et al, 2010). Image 8 was taken with VLTI using MIRA (Le Bouquin et al, 2009). These images are an illustration of how image reconstruction can retrieve moderately complex morphologies with a limited (u, v) coverage that might have escaped traditional model fitting strategies.

Spectral phase referencing has proven to be a powerful tool to image line emitting regions. For this purpose, a sufficient spectral resolution is required in order to compare purely continuum emission to line emission interferometric observables. Results using this technique are illustrated in images 10 and 11 of Fig. 2 where the H_α emission around the star β Lyrae has been mapped using the AIPS package (Schmitt et al, 2009). This was possible because each baseline phase corresponding to the line emission was isolated from the continuum. In a similar spirit, Millour et al (2011) have used AMBER with high spectral resolution, MIRA, and a self-calibration approach to retrieve absolute phases in the Br γ line

of the supergiant HD 62623. Since the line was both spectrally and spatially resolved it was possible to reveal the kinematics of a disk around the central star.

Mapping the infrared emission of protoplanetary disks has always been one of the key science drivers for optical arrays and their focal instrumentation. Images 12 to 14 of Fig. 2 are an illustration of the best disks maps achieved so far in this field. Images 12,13,14 have been obtained, respectively, by Aperture Masking at Keck (Tuthill et al, 2002) and long baseline interferometry at VLTI (Kraus et al, 2010; Benisty et al, 2011). Images 12 and 14 clearly show the inner rim of the circumstellar disk caused by dust sublimation. Maps 13 (using the BBM method) and 14 (using MIRA) display limited features in the image because of the relatively sparse (u, v) coverage obtained with the VLTI.

The images obtained with aperture masking at Keck by Tuthill et al (1999, Wolf-Rayet 104) and Monnier et al (2004, Evolved star NML Cyg) show the most complex features of all the images selected here (images 15-17 of Fig. 2). This complexity is a direct illustration of the importance of a sufficient (u, v) coverage since both used masks with 21 apertures. MEM priors were chosen in the reconstruction process. The case of the NML Cyg map is also very illustrative of the requirement to strategically pave the (u, v) plane. Therefore, one should always consider complementing long-baseline interferometry with single-dish aperture masking if possible or vice-versa. In this particular case, the Keck aperture masking data lacked high spatial frequency constraints on the central source (left image). The addition of IOTA data allowed the central source extension to be characterized and improved the quality of the reconstruction. Conversely, extended fluxes might alter interferometric data and should therefore be at least calibrated and ideally measured with short spatial frequency instruments such as aperture masking instruments.

3 The future of aperture synthesis: astrophysical objects at the milli-arcsecond scale

While optical long baseline interferometers have made tremendous technical and scientific progress, we wanted to evaluate what improvements could be brought to the field of aperture synthesis imaging. Following the recommendations of the SOC supervising the *Workshop on Interferometric Imaging 2009* (see acknowledgements), we selected four main astrophysical topics for which visible and infrared interferometers are expected to bring breakthroughs and for which milli-arcsecond scale imaging will certainly improve our understanding of the physical phenomena. We restricted ourselves to the study of the continuum emission of various object classes. The following sections detail those topics.

3.1 Planetary signatures in protoplanetary disks

3.1.1 Context and major issues

Currently⁴, more than 700 exoplanets⁵ together with several thousand of planet candidates have been detected so far and although the detection techniques used may cause strong selection effects, it is now obvious that the solar-system planets cover a small region in the parameter space of possible planetary characteristics. To understand the observed diversity of planets, one has to consider the history of the planetary systems by studying their formation

⁴ as of December 2011

⁵ <http://exoplanet.eu>

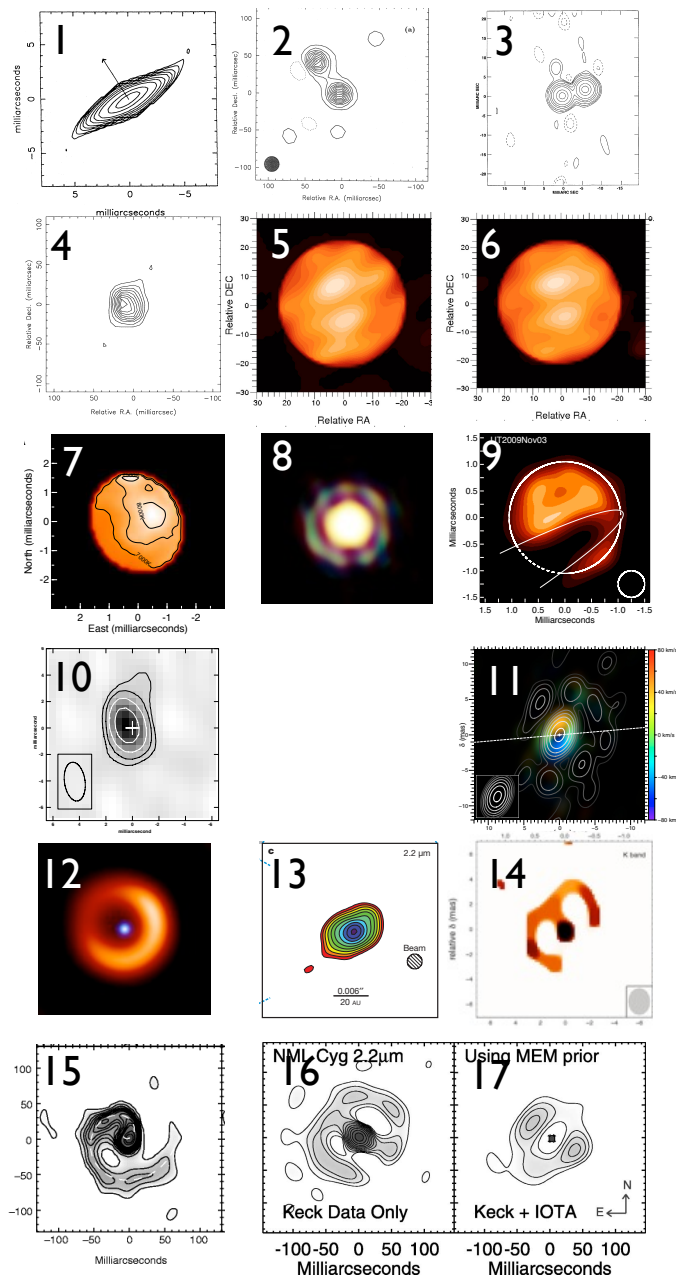


Fig. 2 The wall: examples of published reconstructed images (see text for details). 1:Quirrenbach et al (1994) 2:Baldwin et al (1996) 3:Benson et al (1997) 4:Young et al (2000) 5&6 Haubois et al (2009) 7:Monnier et al (2007),8: Le Bouquin et al (2009), 9:Kloppenborg et al (2010),10:Schmitt et al (2009), 11: Millour et al (2011),12:Tuthill et al (2002), 13:Kraus et al (2010), 14:Benisty et al (2011), 15 Tuthill et al (1999), 16&17 Monnier et al (2004). Credit for figure 8: ESO/J.-B. Le Bouquin et al.

and evolution. Triggered and supported by the rapidly growing field of the search for extra-solar planets and the observational material already collected, our theoretical understanding about the planet formation process has been improved significantly. Nevertheless, the link between theoretical models and observations is still rather weak. This link is provided by circumstellar disks in which planets are expected to form. These disks are considered as the natural outcome of the protostellar evolution, at least in the case of low and intermediate mass stars (e.g. Adams et al, 1987; Lissauer, 1993). These disks have masses ($10^{-3} - 1 M_{\odot}$; Beckwith et al, 1990) and sizes (50 – 1000 AU; McCaughrean and O’Dell, 1996; Dutrey et al, 1996) comparable to those expected for the primitive solar nebula.

Theoretical investigations show that the planet-disk interaction creates structures in young circumstellar disks which are usually much larger in size than the planet itself and thus more easily detectable (Masset and Papaloizou, 2003; Varnière et al, 2004; Crida and Morbidelli, 2007). The specific result of the planet-disk interaction depends on the evolutionary stage of the disk. Typical signatures of planets embedded in disks are gaps and spiral density waves in the case of young, gas-rich protoplanetary disks, and characteristic asymmetric density patterns in older debris disks. Numerical simulations demonstrate that high-resolution imaging performed with observational facilities (already existing or soon becoming available) will allow these “fingerprints” of planets to be traced in protoplanetary and debris disks (e.g. Wolf and D’Angelo, 2005) but the prospect of such detections lies mostly in the mm domain. These observations will provide a deep insight into specific phases of the formation and early evolution of planets in circumstellar disks. For example, Wolf and Klahr (2002) showed that the Atacama Large Millimeter Array (ALMA) will allow tracing of hyper-dense vortices which are supposed to represent an early stage of planet formation. Some authors have tested the detectability of planet-induced features, such as temperature increase due to planetary accretion, in the near-to-mid-infrared domain with interferometers (e.g. Wolf, 2008) and have already pointed out that this represents a major challenge. These studies have to be pursued.

For this work we wanted to test the limit of the planet-induced structures that could be detected. We have therefore not considered other crucial observational diagnostics that could also (and already do) allow the properties of protoplanetary environments at the astronomical unit scale to be further constrained. These observable diagnostics include the disk inner rim vertical structure, the dust content and its vertical distribution, kinematics, asymmetries etc. Since these are already the subject of active research we instead chose to investigate more challenging observables which could become accessible in the future.

3.1.2 Simulated images of disks perturbed by planets

The model for radiative transfer in the vicinity of an embedded protoplanet used in this work is detailed in Jang-Condell (2008). It is based on a one-dimensional analytical solution for radiative transfer in an optically thick protoplanetary disk (D’Alessio et al, 1998) extended to three dimensions. The calculation is carried out iteratively for self-consistency between temperature and density perturbations. The generation of simulated images is described in Jang-Condell (2009).

The synthetic image produced for the image reconstruction is of a face-on disk at a distance of 140 pc. Since the simulation boundaries are limited in radius at both the inner and outer edges, the disk brightness is smoothly extrapolated as a power-law interior and exterior to the simulated region in order to eliminate image edge artifacts. The star is modeled as a black body of radius $R_* = 2.6 R_{\odot}$ and effective temperature $T = 4280$ K, corresponding to a 1 Myr old star of mass $M_* = 1 M_{\odot}$ (Siess et al, 2000).

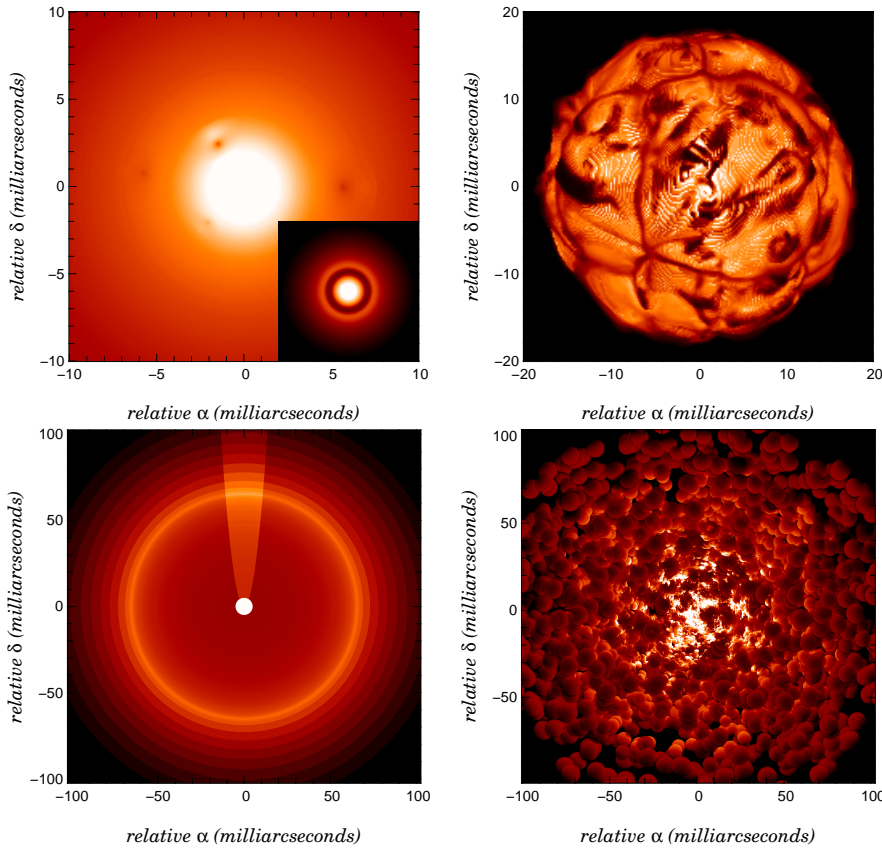


Fig. 3 Simulated images of our 4 science cases. Top, left to right: (a) disk in the N band with shadows created by low-mass embedded planets (Sect. 3.1.2), inset shows disk with gap in the N band; (b) stellar surface of a supergiant star with convective cells in the K band (Sect. 3.2.2). Bottom, left to right: (c) evolved star with surrounding multi-layer envelope and plume emission in the K band (Sect. 3.3); (d) a clumpy dust torus in the active galactic nuclei NGC1068 in the K band (Sect. 3.4.2). The simulated images are presented in their largest field of view when available.

The first set of images consisted of planets (top left image of Fig. 3) creating localized shadows (Jang-Condell, 2009): (i) 10 and 20 M_{\oplus} planets at 8 AU, (ii) 10 and 50 M_{\oplus} planets at 4 AU, (iii) a 20 M_{\oplus} planet at 2 AU, and (iv) a 50 M_{\oplus} planet at 1 AU. All these planets are present in the image. The second set of images (inset of the top left image of Fig. 3) were of gaps created by tidal forces between the planet and disks, similar to those shown in hydrodynamic simulations by Bate et al (2003). These gaps were modeled as *ad-hoc* azimuthally-symmetric perturbations. If the unperturbed surface density profile is defined as $\Sigma_0(r) = \int_{-\infty}^{\infty} \rho(r, z) dz$ then the surface density profile of a disk with a gap whose center is located at radial distance r_g of depth d and width w is $\Sigma = \Sigma_0[1 - d \exp(-(r - r_g)^2/2w^2)]$. Holding Σ fixed, the vertical density and temperature structures were recalculated using the radiative transfer model described above. Two images of a gap at $r_g = 10$ AU was calculated: (1) “big gap” scenario with $d = 0.9$ and $w = 1.8$ AU, corresponding to a 110 M_{\oplus} (0.35 M_J) planet; and (2) “small gap” scenario with $d = 0.5$ and $w = 1.0$ AU, corresponding to a 37 M_{\oplus} (0.12 M_J) planet.

3.2 Granulation in late-type stars due to large convective cells

3.2.1 Context and major issues

Outside the spots, the solar surface is covered by bright granules with warm upflowing material surrounded by dark, cool inter-granular lanes where matter falls downward. Local multi-dimensional radiation hydrodynamics (RHD) simulations of stellar surface convection, solving the coupled equations of hydrodynamics and non-local radiation transport including constant gravity, ionization effects, and realistic (binned) opacities, first successfully reproduced the properties of solar granulation (Nordlund, 1982). This includes pattern and dynamics (incl. size and timescales) of the granulation, as well as center-to-limb variation, and line profiles (Dravins et al, 1981). The excellent agreement between observations and models allowed these methods to be extended with some confidence to other stars, replacing classical 1D stellar atmospheres for high-accuracy abundance determinations (Allende Prieto et al, 2001; Caffau et al, 2008).

The size and also the contrast of the surface structures can be directly linked to the efficiency of convection, to the formation of molecular lines (CO on the Sun: Wedemeyer-Böhm et al 2005; water on Arcturus: Ryde et al 2002; water on Betelgeuse: Ryde et al 2006), to the micro-variability (limiting the detectability of planets Ludwig, 2006) and to the vertical extent of “overshoot” of convective influence (Freytag et al, 1996) into the outer layers (molsphere, wind: Sect. 3.3; and dust formation: Freytag and Höfner 2008).

Simulations of solar-type stars show the granulation properties known from the Sun, with a horizontal size scaled with the surface pressure scale height and slightly different contrast (e.g. Robinson et al, 2004). However, the situation changes for objects near the “granulation boundary” (A-type stars, cepheids, red supergiants): Gray (2008) observes reversed C-shaped line bisectors on Betelgeuse and relates them to granulation and giant convection cells accompanied by short-lived oscillations. Also Stothers and Leung (1971) and Schwarzschild (1975) attribute the observed photometric variability in red supergiants to convection cells larger than one would expect from scaled solar granulation, which is confirmed later by interferometric observations of global surface structures on Betelgeuse (Buscher et al, 1990; Young et al, 2000). Josselin and Plez (2007) find large line shifts and asymmetries in RSG spectra and attribute them to the existence and motion of a few large granules. Local RHD models of surface patches of A-type stars and cepheids (Freytag et al, 2008) and global models of red supergiants (using a spherical potential and including the entire outer convective envelope and the atmosphere, Freytag et al 2002) also show similarly large cells and granulation with properties deviating from the solar case.

For a large group of stars near the granulation boundary – from the main-sequence to red supergiants – our benchmark star, the Sun, is therefore no longer useful. There is a clear need for new references, and interferometric imaging will be capable of providing one for the important case of red supergiants, shedding light on this particular kind of surface granulation and its relation e.g. to the outer layers and wind formation. Recent images of Betelgeuse obtained with IOTA in the *H* band (Haubois et al, 2009) display two low contrast spots, one of them probably marginally resolved. The spots are consistent with signatures of large convective cells (Chiavassa et al, 2009).

3.2.2 Stellar surface simulation

Chiavassa et al (2009) computed intensity maps at different wavelengths (corresponding to broadband filters *H* and *K*) with the radiative transfer code OPTIM3D from snapshots

of the 3D hydrodynamical simulation (code CO⁵BOLD) of a red supergiant star presented above. They used a model with stellar parameters close to those of Betelgeuse (Levesque et al, 2005): a $12 M_{\odot}$ stellar mass, a luminosity averaged over time of $L = 93000 \pm 1300 L_{\odot}$, an effective temperature of $T_{\text{eff}} = 3490\text{K}$, a radius of $R = 832R_{\odot}$, and surface gravity $\log(g) = -0.337$. The numerical resolution is 235^3 with a grid spacing of $8.6R_{\odot}$.

The granulation pattern has a significant impact on interferometric observables. In order to derive their characteristic signature, Chiavassa et al (2009) computed visibilities and closure phases from these intensity maps. They found that convection-related surface structures cause fluctuations in interferometric observables which manifest themselves mostly at high spatial frequencies after the first null point in the visibility function. In general, the visibilities and closure phases deviate greatly from the uniform disk or limb-darkened cases, due to the small scale structure on the model stellar disk. These observables have been compared to existing Betelgeuse observations (Young et al, 2000, 2004; Haubois et al, 2009). The 3D simulation gives good fits to the observed visibility points and closure phases providing a consistent solid detection and characterization of the granulation pattern from the optical to the near-infrared (Chiavassa et al, 2010).

The granulation pattern can be characterized with today's interferometers by searching for angular or temporal visibility fluctuations or by looking at different spectral regions corresponding to spectral features and continuum. High-angular resolution images should verify or contradict the 3D simulations in terms of surface intensity contrast, granulation size and temporal variation. The figure at the top right side of Fig. 3 shows the image, computed in a narrow K band channel, that has been used in this study.

3.3 Molecular layers around late-type stars

3.3.1 Context and major issues

The late stages of stellar evolution are well studied because they are the source of most of the dust produced in the universe (Sedlmayr, 1994). Dust is detected at large distances and stars are known to produce molecules which are the building blocks of dust particles. A molecular shell containing water vapor and carbon monoxide was first suspected around red supergiants by Tsuji (2000) who coined the name *molsphere* to describe it. This explanation was shown to be consistent with interferometric data collected in the near and mid-infrared (Perrin et al, 2004a; Weiner, 2004; Ohnaka, 2004) and subsequent works showed the list of molecules could be further extended to include SiO and Al₂O₃, the latter being a dust species that can survive the high temperature range of the *molsphere* (1500–2000 K) and provide nucleation sites for SiO (Perrin et al, 2007; Verhoelst et al, 2006).

Molecules in the atmosphere of Mira stars are probably lifted by large-amplitude pulsations. This is possibly a different process from the one at play in supergiants, yet similarities have been found between the two classes of objects. Diameters of Mira stars are known to vary by factors of a few in and out of TiO bands (e.g. Labeyrie et al, 1977) as well as in other bands although with smaller amplitude. Measured interferometric diameters have been difficult to explain with models partly because of pulsations. Some dynamic models have been compared to interferometric data (e.g. Woodruff et al, 2004; Fedele et al, 2005). Using the Scholz and Takeda (1987) model and removing the contribution of the continuum in the K band, Perrin et al (1999) have shown a good agreement with R Leo interferometric data raising the hypothesis that molecules are a major contributor to the infrared surface brightness distribution of these objects. This was confirmed by fitting K and L band data

using a model incorporating a molecular shell a stellar radius above the photosphere (Mennesson et al, 2002; Perrin et al, 2004b). Recent works have provided more detailed studies of the shell (e.g. Ohnaka et al (2005); Eisner et al (2007); Wittkowski et al (2007); Ohnaka et al (2009)). In parallel models have been made more sophisticated and in particular now provide a physical explanation for molospheres (Woitke et al, 1999).

All studies had initially hypothesized circular symmetry and homogeneity for the layer. Images would yield a refinement of the structure of the layer and of the star, as well as the layer brightness distribution. The images of T Leporis in narrow spectral channels across the H and K bands taken with VLTI (Le Bouquin et al, 2009) have confirmed the presence of the circumstellar layer. The ring appears circularly uniform to within the precision of image reconstruction with sparse apertures, consistent with the type of shell model proposed by Perrin et al (2004b). Images taken with IOTA of χ Cygni in the H band do not disclose such a bright shell, although it is detected by model-fitting to visibilities. The star itself shows varying asymmetries as a function of the pulsation phase (Lacour et al, 2009). However insufficient dynamic range in the reconstructed image does not allow any departure from circular symmetry of the shell to be measured.

3.3.2 Modeling molecular layers

Interferometric observations (and thus also reconstructed images) of molecular layers can be compared either to self-consistent (hydrodynamical) atmosphere models, or to flexible analytical models which aim at a reproduction of the observed intensity distribution with a minimum of physics.

The first approach works reasonably well for Mira stars. For example, Wittkowski et al (2008) use the models by Ireland et al (2004), and Woodruff et al (2009) use the models by Keller and Wood (2006), both on O-rich AGB stars. Theoretical preparatory work on C-rich AGB stars has been published by Paladini et al (2009), based on models by Höfner et al (2003), and a confrontation with observations is in progress (Sacuto et al, 2011).

In some cases, a more ad-hoc approach is required. This usually implies a parametrized distribution of matter and opacity, and some radiative transfer calculation. These models should then be checked against thermal and chemical equilibrium. Such an approach has also been used with AGB star observations (e.g. Mennesson et al, 2002; Perrin et al, 2004b; Le Bouquin et al, 2009), but it is hitherto the only option for red supergiant stars (e.g. Verhoelst et al, 2006; Ohnaka et al, 2008), or very asymmetrical circumstellar environments (Kervella et al, 2009).

The synthetic images used in this work consist of an RSG photosphere model, computed with the MARCS code (Gustafsson et al, 1975, and further updates), surrounded by two layers of molecular material: a layer of CO is located at $1.15 R_{\star}$, with a temperature of 2350 K, and a column density of 10^{23}cm^{-2} . The second layer contains 10^{21}cm^{-2} of H_2O and is located at $1.7 R_{\star}$, with a temperature of 1850 K. Around this object, we placed a dust shell which reproduces the observed silicate features in α Orionis ($\dot{M} \sim 3 \times 10^{-8} M_{\odot} \text{yr}^{-1}$). This shell starts at $13 R_{\star}$, and has a typical r^{-2} outflow density profile. To mimic the recent results of Kervella et al (2009), we included a plume as a characteristic of inhomogeneous mass loss, possibly related to convection, as recently observed in Betelgeuse. The chosen plume shape is a simplification of a structure originating at the photosphere, experiencing dilution as it travels outwards. It represents a local increase of 50% of the circumstellar intensity. Images were computed across the K band, but only the one near $2.4 \mu\text{m}$ is presented here (bottom left side of Fig. 3 and zoomed image at top centre of Fig. 6), as it shows both the CO and the H_2O layer.

3.4 Dusty tori in active galactic nuclei

3.4.1 Context and major issues

Although there are numerous classes of active galactic nuclei (AGN), they have been unified into a single scheme (e.g., Antonucci, 1993, 2002; Urry and Padovani, 1995). The basic premise of unification is that every AGN is intrinsically the same object: a super-massive black hole whose activity is powered by accretion through a surrounding disk. This central engine is further surrounded by a dusty toroidal structure, which provides anisotropic obscuration of the central region. The observed diversity is simply the result of viewing this axisymmetric geometry from different angles. Directions with clear sight of the central engine yield “type 1” objects, where clouds in close proximity to the black hole, moving at high velocities because of the strong central gravity and ionized by the strong central continuum radiation, give rise to broad line emission in high ionization lines. AGN whose central engine and broad-line region (BLR) are blocked from view are “type 2”.

The primary evidence for the torus arose from spectropolarimetric observations of type 2 sources, which reveal hidden type-1 emission via reflection off material situated above the torus opening. While compelling, this evidence is only indirect in that it involves obscuration, not direct emission by the torus itself. Direct evidence comes from IR observations — an obscuring dusty torus should reradiate in the IR the fraction of nuclear luminosity it absorbs, and the continua from most AGN indeed show significant IR emission. Recent progress in IR high-angular resolution techniques achieved direct imaging (e.g. Weigelt et al, 2004) and interferometric measurements (Jaffe et al, 2004; Meisenheimer et al, 2007; Tristram et al, 2007) of the torus in a few AGN. These observations show that the torus is rather compact. The size scale is set by the dust sublimation radius $R_d \approx 0.4 (L/10^{45} \text{ erg s}^{-1})^{1/2}$ pc, which determines the torus inner radius. All observations are consistent with R_{out}/R_d no larger than $\sim 20\text{--}30$, and perhaps even only $\sim 5\text{--}10$. The observations also indicate close proximity between dusty regions with widely different temperatures. These findings can only be understood if the dust distribution is clumpy because in that case the dust temperature is much higher on the illuminated face of an optically thick cloud than any other part of its surface, resulting in co-location of different dust temperatures. The torus clumpiness, predicted early on by Krolik and Begelman (1988), naturally explains many features of the IR observations that cannot be understood in smooth-density models (Nenkova et al, 2002; Elitzur, 2008; Nenkova et al, 2008a,b).

3.4.2 Clumpy tori simulations

We simulated model images based on 3D clumpy torus models (Hönig et al, 2006; Hönig and Kishimoto, 2010). The main parameters of the models are (1) the radial dust distribution, parametrized as a power-law $\eta(r) \propto r^a$, (2) the mean number of clouds N_0 along an equatorial line-of-sight, and (3) the half-opening angle θ_0 (defined as σ in a Gaussian distribution along the altitudinal direction). The inner radius of the torus R_d is set by dust sublimation at temperature $T_{\text{sub}} = 1500$ K and scales with the luminosity of the AGN, $R_d \propto L^{1/2}$. While the model spectral energy distribution (SED) has a negligible dependence on the actual size of the dust clouds (see Hönig and Kishimoto, 2010, Sect. 2.5), the clouds might show up in the interferometric signal as small-scale emission or obscuration regions. The cloud sizes are parametrized by a radial power-law.

Starting from pre-calculated databases, clouds are randomly distributed within the torus. Each cloud is associated with a corresponding cloud in the database of directly- or indirectly-

Table 2 Imaging interferometers in use or in construction.

Facility	Wavelength (microns)	Numbers of apertures	Aperture (m)	Baseline (m)
NOI	0.45 – 8.5	6	0.12	2 – 99(437)
CHARA	0.5 – 2.5	6	1	50 – 330
VLTI	1 – 13	4	8.2	40 – 130
	1 – 13	4	1.8	8 – 200
MROI*	1 – 2.5	10	1.4	7.5 – 350

* in construction

illuminated clouds, the cloud image is placed in the model space, and images at all spectral channels are computed using the obscuration along the observer line-of-sight. The simulations are performed for a torus which is seen edge-on by the observer, as we would expect in a type 2 AGN, located at the distance of NGC 1068, the only AGN with published interferometric data in both near- and mid-IR (Weigelt et al, 2004; Wittkowski et al, 2004; Jaffe et al, 2004; Raban et al, 2009) which is close enough so that clumpiness in the torus can be observed (see the right image of Fig. 3 to get a wide view of the simulated AGN and the top right image of Fig. 6 to get a zoom on the central part). For that simulation we did not take into account the incoherent flux contribution from the surrounding galaxy which will bias the measurements. We discuss this issue further in Section 6.1.4.

4 Available imaging facilities

NOI, CHARA, VLTI, and MROI are the present and near-future interferometers which can perform image synthesis (see Table 2). We used their configurations to produce realistic simulated reconstructed images for the astrophysical topics described in Sect. 3. We describe below the main characteristics of these instruments and their most recent imaging results.

4.1 CHARA

The Center for High-Angular Resolution Astronomy (CHARA) Array is a 6 telescope interferometer operated by Georgia State University on the Mt. Wilson site outside Los Angeles, California (ten Brummelaar et al, 2005). CHARA has the longest baselines of any current optical interferometer (maximum 330m baseline), allowing sub-milli-arcsecond angular resolution in the visible and infrared. While most of the 30 CHARA refereed papers to date present infrared observations using only single baseline data (e.g., McAlister et al, 2005), we focus here on progress in *imaging* which requires at least 3 telescopes to be used.

Currently, the only combiner at CHARA to have published imaging results is the Michigan Infrared Combiner (MIRC, Monnier et al, 2006). MIRC now combines up to 6 CHARA telescopes simultaneously and can produce snapshot images of stellar surfaces and interacting binaries, as long as the surface features are not too complicated. Monnier et al (2007) presented a detailed image of the star Altair, the first resolved image of a main-sequence star, confirming the strong gravity darkening and oblateness expected for this rapid rotator. The rapid rotators Alderamin and Rasalhague have now also been imaged and modeled by CHARA (Zhao et al, 2009). Another breakthrough made possible by imaging was the

first “movie” of the interacting binary β Lyrae (Zhao et al, 2008), imaging the pair of stars through half of the ~ 13 day orbital period. More recently impressive images of the well known eclipsing system ϵ Aurigae revealed the transiting shadow of a flat disk (Kloppenborg et al, 2010). New imaging targets include the gas disks of Be stars and rotating spots on active stars.

Imaging efforts at CHARA are rapidly intensifying with the recent commissioning of the PAVO and VEGA combiners, both visible combiners capable of closure phase measurements and interferometric imaging. A 6-telescope fringe tracker (CHAMP) has been delivered in Summer 2009 and the 2-telescope CLASSIC combiner has been upgraded to use three telescopes (CLIMB). MIRC is starting to use all six CHARA telescopes simultaneously allowing the imaging of planet-forming disks in young stellar objects for the first time.

4.2 VLTI

The Very Large Telescope Interferometer (VLTI, Haguenaer et al, 2008) is located at Cerro Paranal, Chile, and is operated by the European Southern Observatory. The infrastructure is composed of four relocatable 1.8m Auxiliary Telescopes (ATs) equipped with visible-wavelength tip/tilt correction, four fixed 8.2m Unit Telescopes (UTs) equipped with visible-wavelength adaptive optics, and 6 delay lines of 100 m stroke. The minimum baseline is 8m while the maximum one is about 200m. The focal laboratory is equipped with a JHK -band 3-beam combiner AMBER (Petrov et al, 2007) allowing precise measurements of closure-phases, and with an N -band 2-beam combiner MIDI (Leinert et al, 2003). The VLTI instruments are opened to the astronomical community thanks to dedicated observatory support, leading to a total of more than 191 refereed papers in 8 years (2004–2011).

The first reconstructed image produced by the VLTI is of the binary θ^1 Ori C (Kraus et al, 2009), using three configurations of 3 ATs. The spectral coverage of AMBER across the K -band was used to enhance the coverage of the (u, v) plane. However because observations were not close enough in time, the authors had to artificially “rotate” the (u, v) plane between each configuration to account for the binary rotation. Almost at the same time, Le Bouquin et al (2009) reconstructed a spectro-image of the Mira variable T Lep at a spectral resolution $R \sim 35$ using AMBER and four 3-AT configurations. Using the MIDI instrument with the 6 possible UT baselines, Raban et al (2009) reconstructed an image of the torus at the heart of NGC 1068. The image is point-symmetric because of the lack of phase information. Other imaging works are in progress concerning B[e] stars (Millour et al, 2009), young stellar objects and supergiants.

ESO is currently commissioning PRIMA (Delplancke et al, 2006), an instrument which will be able to simultaneously observe two stars separated by up to an arc minute, using 2 telescopes. Beyond the astrometric capability which is the primary focus of PRIMA, it will allow differential phase measurement and possibly an improvement in absolute phase measurements for imaging. The fringe sensors that come with it are also expected to be more sensitive. Since October 2011 a visitor instrument PIONIER allows four VLTI telescopes (ATs or UTs) to be combined and has provided first images of interacting binaries (Le Bouquin et al, 2011; Blind et al, 2011b; Berger et al, 2010). Around 2013, the VLTI is expected to receive the first second-generation general user instruments making use of 4 telescopes simultaneously. These are Matisse working in the L, M, N bands (Lopez et al, 2008) and Gravity with dual beam operation and an astrometric capability (Eisenhauer et al, 2008).

Later, it is planned that the VSI instrument will eventually combine 6 or even 8 telescopes simultaneously, providing realistic snapshot imaging capability (Malbet et al, 2008). In parallel, phase A studies of a second generation fringe-tracking instrument, capable of cophasing an array of 4 and potential more telescopes are being conducted. This instrument will be essential to improve the sensitivity of second generation science combiners (Meisner et al, 2010; Blind et al, 2011a).

4.3 MROI

Located in New Mexico (USA), the Magdalena Ridge Observatory Interferometer (MROI, Creech-Eakman et al, 2008) is a visible and infrared telescope array under construction. MROI will comprise ten 1.4-m diameter unit telescopes laid out in a Y-shaped array. The telescopes will be relocated approximately three times per year. Four scaled array configurations will be available, the most compact configuration giving *shortest* baselines of 7.8 m for comparison with single-dish measurements, and the most extended configuration having a longest baseline of 340 m.

MROI has been designed for model-independent imaging of faint targets with a layout optimized for baseline bootstrapping employing equal spacings between adjacent telescopes on each array arm, essentially 100% sky coverage down to 60 deg from zenith, a beam train that minimizes the number of optical surfaces encountered by the light beams, and a group-delay fringe tracking capability, with limiting point-source sensitivity of $H = 14$.

First light is expected in 2012, with first fringes in 2013. Phase A deployment (6 telescopes and the *JHK* science capability) could be completed as soon as 2015. Phase B (10 telescopes and optical science) will begin when more funding for unit telescopes, associated delay lines and an optical beam combiner is obtained.

4.4 NOI

NOI (ex NPOI⁶) has pioneered aperture synthesis in the optical domain and is still operational today with active plans for future developments (Armstrong et al, 1998b; Hutter et al, 2008). The array has two subarrays dedicated to imaging and astrometry. While the imaging array uses 12 cm beam-stopped relocatable siderostats it will eventually use six siderostats of 35 cm aperture. The astrometric subarray is composed of six 50 cm siderostats with shorter baselines (19 to 38 m). The focal instrumentation operates in the 450 nm to 850 nm band. The current imaging capability is obtained through the combination of two “imaging” siderostats with four of the astrometric ones. NPOI offers the unique feature of being able to maintain active group delay fringe tracking for its 6 siderostat operation therefore offering a unique snapshot imaging capability. The current maximum operational baseline for imaging is 99 m but the array will have the capability to span baselines from 2 to 437 meters. The integration of the former Keck-interferometer 1.8 m telescope outriggers to the imaging array is under study. In parallel a study to install 1.4 m composite telescopes equipped with adaptive optics is underway with the first step being construction of a prototype. Since 1998 NPOI has been particularly successful at improving its automation (in particular in the field of array-phasing), studying binary systems of various types, and demonstrating a spectral phase referencing capability (e.g. Benson et al, 1997; Zavala et al, 2010; Schmitt et al, 2009).

⁶ Navy Prototype Optical Interferometer

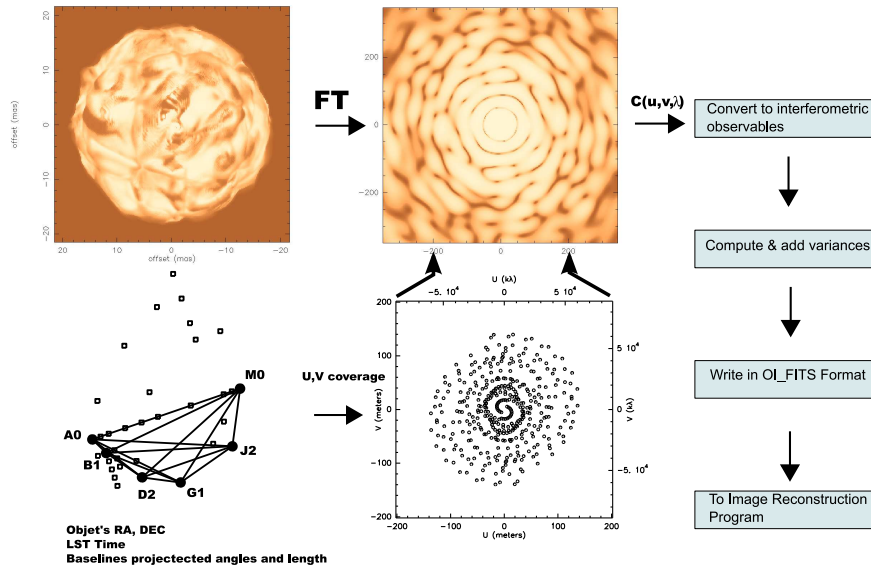


Fig. 4 From an image to visibilities: Modeling interferometric observables with ASPRO.

5 Results from image reconstruction simulations

In this section we first describe the method for generating realistic interferometric data from the MROI and VLTI, utilizing the telescope relocation capability of these facilities. Then we show the images that were reconstructed by our colleagues without prior knowledge of the scientific content. Finally we compare the reconstructed images with the original ones and discuss our findings.

5.1 Simulating realistic interferometry data

The simulations used here have been made with the ASPRO package (Duvert et al, 2002). ASPRO is a general-purpose observation preparation tool developed by the *Jean-Marie Mariotti Center*⁷ for optical interferometers, with a particular emphasis on the VLTI instruments (Sect. 4.2). ASPRO and its little brother ASPRO2 are available as a web-based utility, with a client-server architecture and a Java user interface, at <http://jmcc.fr>, and also as a standalone program. ASPRO simulates the observation by an interferometer of an astronomical object, at one or several times, and delivers simulated interferometric observables in the OIFITS format (Pauls et al, 2005).

The interferometric chain is modeled as the combination of an interferometer infrastructure and focal instruments. The interferometer infrastructure comprises the telescopes, delay lines, tip-tilt correctors, adaptive optics, and fringe trackers. It adds geometrical requirements such as the positions and sizes of the telescopes apertures at the time of observation with respect to the position of the science object and the geometrical delays thus induced between each pair of telescopes. In addition, it includes environmental constraints such as

⁷ The JMMC is a network of French laboratories specialized in optical interferometry techniques.

the atmospheric seeing, the different horizons seen by telescopes and technical limitations (limits on the delay-line strokes, flux dependence on the performance of active optical elements...). For each interferometer simulated in ASPRO these requirements are known and tabulated; only the atmospheric seeing (and its associated coherence time) is a variable factor that can be adjusted by the user.

The focal instrument is described by its spectral capability (bandwidth, resolution, number of spectral channels, central wavelength, photometric band...) and its sensitivity and throughput. The former are, for most instruments, fixed as a list of instrumental “modes”. For example, for AMBER, there are 18 such modes, one giving simultaneous J , H , K observations at 35 resolution, 3 for medium (1500) resolution in H or K , and 14 for high (12000) resolution in K . The sensitivity and throughput, i.e., the limiting magnitudes, the visibility losses, the biases and the variance of the values of the various interferometric observables are computed with a dedicated noise model (Appendix A).

The science object is described by its position on the sky and its angular and spectral energy distributions. Those can be either a series of images, one for each wavelength, grouped in a data cube, or a combination of simple analytic models (binary, uniform disk, etc...).

5.2 Simulation methodology

The simulation of observations, depicted in Fig. 4, consists of:

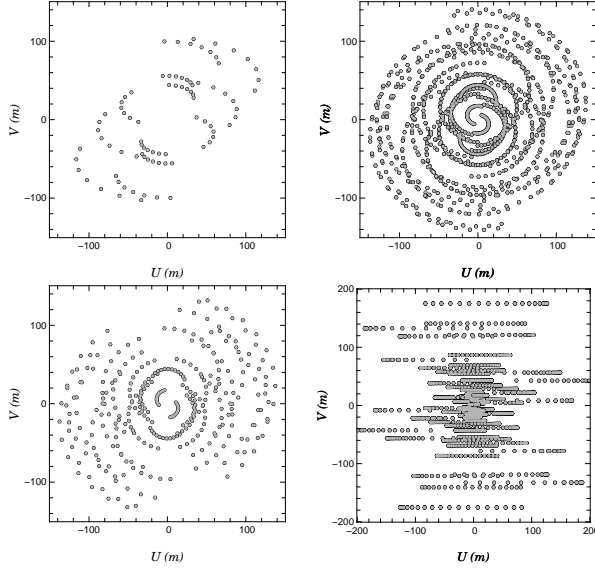
1. building the list of (u, v) positions of the baselines at each wavelength of the required focal instrument mode and at the various times (for example, an observation every 20 minutes for 6 hours around the meridian) intended by the observer;
2. computing the Fourier Transform (FT) of the flux spatial distribution of the object at each wavelength at each (u, v) point defined above (in the present case, where the user provides a model of the object as a cube of images);
3. from the complex visibilities obtained, computing all the interferometric observables, V^2 , amplitude and phase of the bispectrum, and, if the instrument has spectral capabilities, the amplitude and phase of the differential visibility;
4. for each of these interferometric observables, applying the noise model (Appendix A) and a lower-limit accuracy threshold to get the expected variance of each value;
5. randomize the interferometric observables according to their expected variance;
6. export these simulated observations in the OIFITS format.

The (u, v) coverage for both MROI and VLTI was derived from the allowed 6 telescope configurations (Table 3 and Fig. 5). In the case of MROI this was obtained by switching rapidly 6 beams in front of a four beam combiner. This explains why three×four telescope combinations are used to get all 15 baselines.

Undoubtedly, because we do not take into account a detailed model of fringe tracking performances (outside the scope of such a paper), we set ourselves on the optimistic side in terms of calibration biases. We can therefore consider that the images obtained here are the best one can expect from the interferometers and that actual data may contain additional artifacts.

By simulating the expected results of the actual observation and providing OIFITS files, ASPRO allows assessment of not only the feasibility of the observations but also the science potential of the planned observations. The OIFITS file obtained can be used to check whether image reconstruction techniques retrieve the desired information and to compare the results to what a model-fitting software can achieve. The interferometric observables

Array	Configuration
MROI	N2 W2 W4 S2
	N4 W2 W4 S4
	N2 N4 S2 S4
	N4 W4 W6 S4
	N6 W4 W6 S6
	N4 N6 S4 S6
VLTI	A0 B1 D2 G1 J2 M0
	A1 B3 D2 G1 H0 I1
	UT1-UT2-UT3-UT4

Table 3 Array configurations for both MROI and VLTI used in the simulations**Fig. 5** The (u, v) plane coverage used for the image reconstructions. Top from left to right: Matisse/VLTI-UT coverage for the protoplanetary disk model; VSI/VLTI-AT coverage for the late-type supergiant star model for Betelgeuse; VSI/VLTI-AT coverage for the molecular layer model around a late type star; I4/MROI coverage for the dusty tori model for the active galactic nuclei NGC 1068.**Table 4** Description of the parameters of the different science cases

Science cases	Interf.	Instrum.	Wavel.	Algorithm
Protoplanetary disks	VLTI-UT	Matisse	N band	BSMEM
Stellar surface	VLTI-UT	VSI	K band	MIRA
Molecular layers	VLTI-UT	VSI	K band	MIRA
AGN	MROI	I4	K band	BSMEM

Table 5 Number of squared visibilities (V^2), closure phases (CP) and their corresponding average errors over the N_{V^2} , N_{CP^2} measurements. To simulate a potential calibration limit in the minimum visibility and closure phase that could be measured we introduced a threshold of 0.002 in visibility and 0.1 degree in closure phase.

	Disk	Supergiant	Evolved star	AGN
N_{V^2}	42	375	165	972
σ_{V^2}	0.02	0.005	0.01	0.02
N_{CP}	21	250	110	486
σ_{CP}	2°	0.2°	0.3°	1°

can also be compared to the model observables in terms of chi-square distance as a first estimate on the feasibility of the planned observation. Table 5 contains a summary of the computed errors on the visibility and closure phase for the different input images.

5.3 Results

We have performed a series of simulations following the astrophysical prescriptions given in Sect. 3 and using the different instrument configurations described above. We focus our attention on the four cases listed in Table 4, since we chose not to explore all the possibilities, which would have led to more than several tens of results. We have selected results obtained with the instruments VSI/VLTI and I4/MROI in the K band and Matisse/VLTI in the N band. The (u, v) coverage for each configuration is displayed in Fig. 5. The configurations were chosen visually to fill the (u, v) plane as uniformly as possible and therefore ensure the best spatial frequency sampling. For the MATISSE case a fixed UT configuration was used. For the VSI reconstruction two 6 AT telescope configurations were chosen with the supergiant one pushed to the maximum possible hour angle range (e.g. -5h,5h). The MROI coverage corresponded to one of the rare AGN with sufficient angular extension to permit imaging (NGC 1068).

The *Planet signatures in protoplanetary disks* case (hereafter called the protoplanetary disk case) was the only one for which we were not able to retrieve a viable reconstructed image. The conclusion applies both to the embedded-planets image and the disk+gap images. The explanation for this lack of success is that the high contrast between the planet induced gap or shadows and the disk/photosphere emission clearly exceeded the dynamical range achievable with such a technique. None of the cases computed in Sect. 3.1.2 was successful in imaging features beyond the central star, using BSMEM or MACIM. However, the example chosen here is voluntarily an extreme case of imaging. Long-baseline interferometry has already begun to explore imaging of protoplanetary environments (e.g. Benisty et al, 2011) and it is expected that MATISSE will have the ideal combination of sensitivity and angular resolution to reveal the inner morphology of dust emitting inner disks. Possible improvements to the method would be to introduce a multi-wavelength approach. The location of the gap being independent of wavelength continuum observations at various bands might provide additional hints to constrain the gap positioning. We note that recent gaps in transition disks were indirectly revealed by visibility modeling (Benisty et al, 2010; Olofsson et al, 2011).

For the remaining cases the results are summarized in Fig. 6 and Fig. 7 with the simulated images (top row), the simulated images convolved by a Gaussian beam at the maximum interferometer angular resolution (central row), and finally the reconstructed images (bottom row). Figures 8 and 9 show a contour comparison between model and reconstructed image. These figures allow us to carry out the first qualitative comparison between the reconstructed and original images at the proper resolution. For the *Molecular layer around late-type stars* case (hereafter called late-type envelope case) and the *Dusty torus around AGN* case (hereafter called the AGN case), note that the images have been magnified in order to display the central part of the images. In these cases, the image reconstruction was not able to detect the less luminous structures present in a wider field (Fig. 3).

A first visual inspection shows that,

1. for all cases, all the features with flux greater or equal to approximately 1/20 of the peak intensity in the image are roughly correctly positioned and have the correct shape and size;

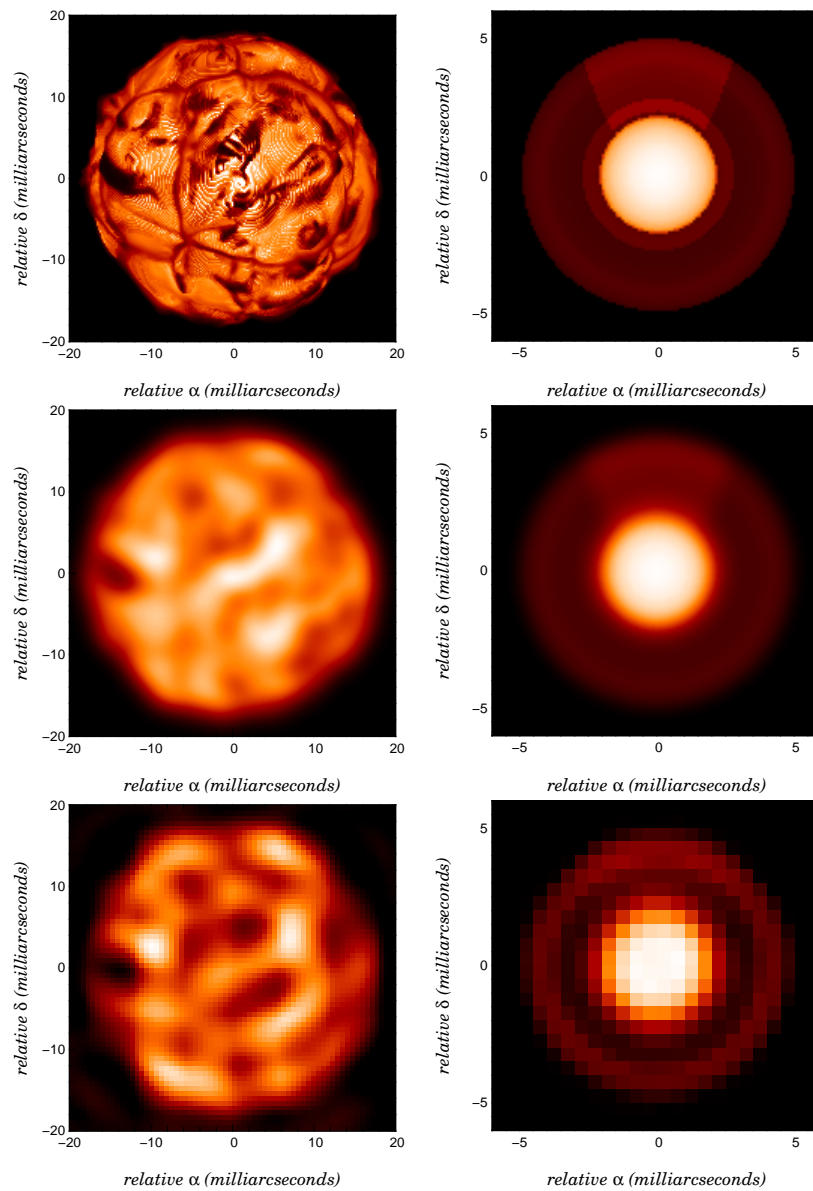


Fig. 6 Resulting images from the image reconstruction (bottom row) of the supergiant (left) and evolved star (right) cases compared to the initial images resulting from our modeling (top row) and compared also to the image that would be obtained by a single telescope whose diameter is the maximum interferometer resolution (central row). The astrophysical cases are on the left column a supergiant star and on the right column a molecular layer around late type star. The color codes correspond to logarithmic scales and the image have been zoomed-in with respect to figure 3 to concentrate on the meaningful reconstructed details.

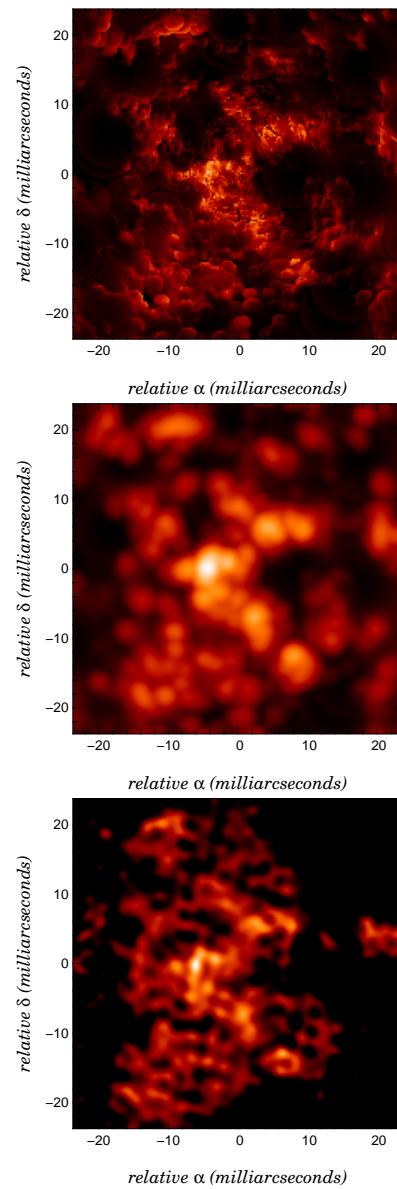


Fig. 7 Resulting images from the image reconstruction (bottom row) of the AGN images compared to the initial images resulting from our modeling (top row) and compared also to the image that would be obtained by a single telescope whose diameter is the maximum interferometer resolution (central row). The astrophysical object is here a dusty tori in active galactic nuclei. The color codes correspond to logarithmic scales.

2. there is evidence that the image reconstruction process brings slightly better resolution than the fringe spacing λ/B which is due to the super resolution allowed by the regularization process and the interferometer response function (this result is best illustrated in the AGN case in Fig. 7);
3. in the supergiant case, the most prominent "granular" atmospheric features are retrieved but the dark thin intergranular lanes of the underlying large-cell convective structure, visible in the model image, are not;
4. in the late-type envelope case the basis of the plume on top center of the image is marginally detected;
5. in the AGN case, the complexity of the scene is obvious and the emission morphology is globally well-reproduced in the reconstructed image. However as we will see later the quantitative interpretation of such an image requires caution.

A proper quantitative comparison cannot rely solely on this visual inspection. For the discussion below, we used one possible image reconstruction quality estimator, called fidelity, described in Appendix B and inspired from ALMA work. There are also valid metrics like the variance of the difference between the two images, reconstructed and original smoothed at the interferometer resolution (Renard et al, 2011) or the figure of merit proposed by Cotton et al (2008) but there is no single metric with proven superiority over all other methods.

6 Discussion

Except for the protoplanetary disk case, optical interferometric imaging is quite successful in retrieving images similar to the *true* images. In this section, we discuss how new and useful astrophysical information can be extracted from interferometric imaging, the similarities and differences with radio-interferometry synthesis imaging, and how to further improve image reconstruction. We conclude with a discussion of how to improve the current facilities to obtain the best information possible using aperture synthesis imaging.

6.1 Getting new and useful astrophysical information

6.1.1 Planetary signatures in protoplanetary disks

High-resolution imaging of protoplanetary disks has the potential to reveal where and when planets form as can be seen on the left image of Fig. 3. Growing cores of giant planets gravitationally and tidally perturb the protoplanetary disks in which they form to create indicators of their presence on scales much larger than the planets themselves, including both localized dimples and azimuthally symmetric gaps. Shadows and brightenings in scattered light images from these perturbations will reveal their presence.

The difficulty in detecting these perturbations using optical interferometry is that the stellar and disk brightness overwhelms the emission from the features in the disk. At millimeter wavelengths, the stellar emission is minimal, so the dynamic range is less of an issue although these wavelengths probe a different regime of the disk as well: the disk becomes optically thin and the images represent vertically integrated thermal emission from the disk. Because of the nature of shadowing and illumination at the surface of the disk, the contrast of the shadows and brightenings is higher at visible and infrared wavelengths as compared to radio wavelengths.

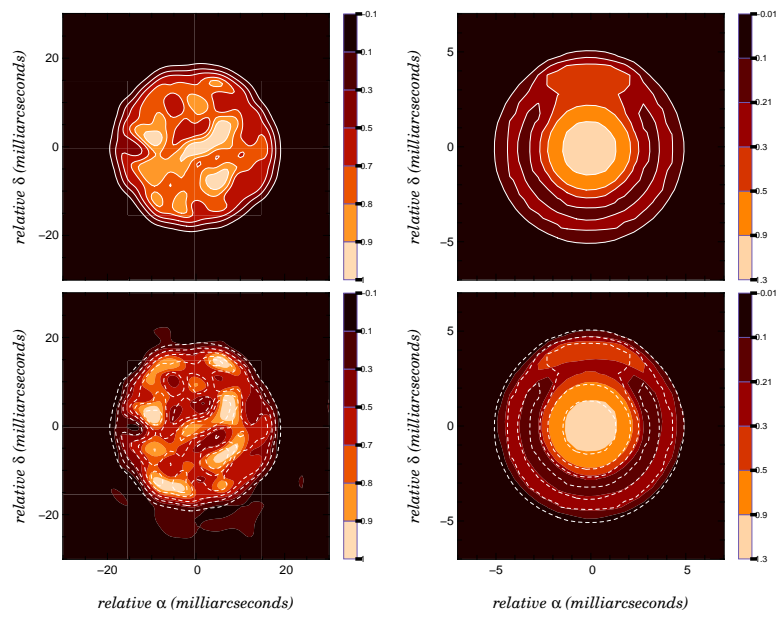


Fig. 8 Contour plots of both original (top row) and reconstructed image (bottom row) for the supergiant case (left) and evolved star with plume (right). Contour levels are expressed in fraction of maximum intensity. Contours of bottom row correspond to the model image for better comparison. Levels: 0.9,0.8,0.7,0.5,0.3,0.1); evolved star with plume (levels: 0.9,0.5,0.3,0.21,0.1).

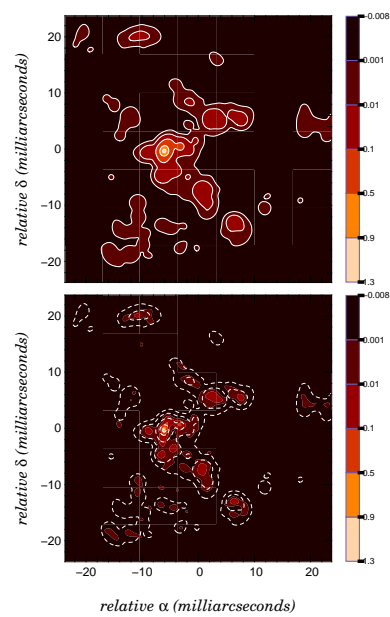


Fig. 9 Contour plots of both original (top row) and reconstructed image (bottom row) in the AGN science case. Contour levels are expressed in fraction of maximum intensity. Contours of bottom row correspond to the model image for better comparison. Levels: 0.9,0.5,0.1,0.01,0.001).

However, these objects can still bring some interesting surprises. In the past, it was believed that disks around young stars would be only marginally resolved by long-baseline optical interferometers in the infrared, but in fact the structures which have been measured are indeed located at larger scales than expected (see review by Millan-Gabet et al, 2007). There might be several other signatures of planets and their formation in the potential planet forming region of circumstellar disks (inner $0.1''$ in nearby star-forming regions): overdense vortices (Wolf and Klahr, 2002); gaps (Wolf et al, 2002; Varnière et al, 2004); accreting giant planets (Wolf and D'Angelo, 2005; Hofmann et al, 2006; Wolf et al, 2007) and other prominent features. Indeed Malbet et al (2005) and Millan-Gabet et al (2006) have reported oscillations in the visibilities that could trace the presence of off-centered hot spots in the disk without identifying its nature. If confirmed, imaging of these relatively bright spots should be relatively easy since the dynamical range quoted in these works ranges between 15 and 50. The failure of our tests reveals that the image reconstructions are limited to dynamic ranges significantly smaller than 10^3 . The reader is referred to Wolf et al (2012) for a detailed review of the potential of long-baseline interferometers for the study of circumstellar disks and planets.

6.1.2 Granulation in late-type stars due to large convective cells

The image we present here was computed in the K band. Chiavassa et al (2009) show that in this spectral region the continuum-forming layers are more visible and the granulation pattern is characterized by large-scale granules of about $400\text{-}500 R_{\odot}$ ($\approx 60\%$ of the stellar radius in Fig. 4 of Chiavassa et al, 2009). On top of these cells, there is small scale structure with characteristic size of $50\text{-}100 R_{\odot}$, $\approx 10\text{-}15\%$ of the stellar radius. This pattern is clearly visible also in the top left panel of Fig. 6.

There are three main characteristics of the granulation pattern that we may try to recover from image reconstruction:

- the size of the granulation cells from the large scale granule to the smaller scale structures;
- the intensity contrast;
- the timescale of the convective motions.

Images of stellar surfaces at various wavelengths will allow these three questions to be answered, and will therefore be a very valuable tool to (in)validate our simulations. This is crucial in order to understand the dynamics of the atmosphere of red supergiant stars, and its importance in, e.g., the still unknown process at the origin of mass-loss (Josselin and Plez, 2007), or in order to determine accurate abundances from spectra using proper model atmospheres.

We compared the original image, smoothed to the interferometer resolution (top left panel of Fig. 6), to the reconstructed image (bottom left panel). The reconstructed image shows medium sized granules, similar to the original smoothed image. There is, however, much more information in the original image, and key features like the large central granule are very hard, if not impossible to see in the smoothed and reconstructed image. This is due to the fact that the emission coming from the inter-granular lanes is too weak compared to the surrounding regions.

We also compared the intensity contrast of the smoothed and reconstructed images by using normalized intensities. For this purpose we normalized the intensity to the peak intensity. The top images of Figures 8 and 9 show for each science case a contour display of the initial images, the bottom ones correspond to contour displays of the reconstructed images.

Comparison can be quantified by measuring the fidelity of the image (Appendix B). We can see that the fidelity of the reconstructed pixels with respect to the original ones can be fairly high (≥ 10) on a significant fraction of pixels (Table 6) but this is unrelated to the interesting stellar surface structures.

Several issues need to be discussed:

- In the K band, it is possible to recover small-to-medium scale granules, while the information about large convective cells is lost. While near-infrared wavelengths have been used in this study, one could consider the interest of studying Red Supergiants in the visible. In the visible, the angular resolution is higher (e.g almost 4 times between the V band than in the K band) and the intensity contrast of granulation is higher. At shorter wavelengths, corresponding to strong molecular absorption, e.g. TiO bands, synthetic intensity maps show more details and much larger contrast between bright and dark areas than in the K band, and larger inter-granular lanes. While pioneering imaging results were carried out using visible instruments (Baldwin et al, 1996; Benson et al, 1997; Young et al, 2000) near infrared wavelengths have been the dominant source of observations because of their lowered sensitivity to atmospheric conditions. However recent developments at CHARA with the VEGA instrument have re-opened the way to such projects (e.g. Mourard et al, 2009).
- Test image reconstructions should be made with interferometers containing more telescopes, or larger baselines, in order to investigate the best affordable way to recover the granulation properties outlined above. As is suggested from comparing simulated images in the visible and near-IR, the right choice of the wavelength may well be a key, despite technical difficulties growing at shorter wavelength.
- Simultaneously to the measurement of the granulation size at different wavelengths, the temporal evolution of the convective pattern should also be compared to the simulations. Extracting typical convection turnover times from series of images should be possible for the medium scales, as soon as the image reconstruction can be trusted, which seems to be the case, even with a small number of telescopes (Fig. 6).

6.1.3 Molecular layers around late-type stars

On a qualitative level, the image reconstruction was successful at detecting the outer molecular shell as a ring-like structure. The base of the plume is also visible, and the wavelength-dependent size of the central object corresponds to the effect of the inner molecular layer. Pixel fidelity computed in Appendix B shows indeed that the stellar-surface pixels are retrieved with a good fidelity (on average 10, while the surrounding layer is less well determined (average fidelity ≈ 5). Our simulation did not include any clumpiness in the circumstellar environment, but the present results indicate that isolated and/or large enough clumps with a contrast of $I_{\text{clump}}/I_{\text{background}} \geq 0.1$ would be detectable. However, the fully resolved extended dust structure could not be detected with the reconstruction algorithms, and the reconstructed limb darkening of the central object is much stronger than that in the input image, making diameter estimates for the central star unreliable and necessitating rather detailed visibility model fitting. Although this has not been investigated at length, we think this is due to the lack of short baselines. Using an image of the star obtained at the diffraction limit of a large telescope when performing the image reconstruction would probably solve this issue like single dish observation in radio astronomy. The latter problem is partly due to an insufficient angular resolution in this particular simulation: Lacour et al (2008) show that the limb darkening can be reconstructed if the data sample the 2nd and 3rd lobe of the

visibility curve, and a limb-darkened prior is chosen for the image reconstruction. Given the highly variable nature of many evolved stars, it is important that real observations come as close as possible to snapshot images.

An evolved star and its circumstellar environments span a huge range in sizes, from convective cells on the surface to the dusty shell at hundreds of stellar radii. Although these different components lead to comparable total flux contributions at IR wavelengths, the difference in size of the radiating surfaces immediately indicates a huge range in intensities. In fact, in our simulated image, the contrast between central star and inner dust shell intensity is $I_{\star}/I_{\text{dustshell}} \sim 10^5$, which is clearly beyond what can be retrieved from the reconstructed image.

6.1.4 Dusty torus in an active galactic nucleus

One of the most interesting tasks for interferometric imaging of AGN dust tori is the characterization of the substructure. At the moment, the actual size of the dust clouds and their properties is closely constrained by SED fitting (Sect. 3.4). However, Wittkowski et al (2004) reported on K -band long-baseline VLTI/VINCI interferometry of NGC 1068 where they found that $\sim 40\%$ of the emission at 46 m baseline is not coming from the larger-scale emission region but confined to scales ≤ 5 mas. Without knowledge of the real distribution of the small-scale flux, this can be interpreted either as emission from the dust-sublimation region or accretion disk, or emission from dust clumps (or “clumping of clumps”) seen through the obscured screen of other clouds (Hönig et al, 2008).

The reconstructed model images of the K -band emission of NGC 1068 show several small emission regions in the central region of the torus. They reflect the parts of the emission from the inner torus region seen through holes in the distribution of clouds at larger radii. The total emission contained in these regions and their sizes are consistent with the constraints from VINCI on NGC 1068. In this way, interferometric imaging allows us to directly detect substructure in the torus and even give an estimate of its contribution to the overall flux of the torus. Interestingly, the analysis of our model images shows that the holes in the obscuring screen of more distant clouds have similar sizes as the typical cloud sizes. If that holds for other model parameters as well, measuring the sizes of the small-scale emission regions might even provide constraints for the typical size of dust clouds in the torus.

When trying to evaluate the fidelity of the pixel intensities with respect to the model images (Appendix B), the fidelity is generally low and while the global morphology of the emitting regions is nicely restored, the intensity of the emitting regions is largely deviating from the original one. This was expected as this image was by far the most complex of our set. Improving intensity accuracy is essential in order to exploit color maps (e.g. $H-K$, $K-L$ or $N-H$) to bring constraints on dust obscuration and the temperature distribution.

An additional issue that was not taken into account is the probable contribution of incoherent flux by the host galaxy. As recognized by Kishimoto et al (2011), particular care will have to be taken in calibrating this flux through SED fitting and, when possible, through single dish measurements such as those provided by aperture masking (e.g. Monnier et al, 2004).

6.2 Similarities and differences with mm-wavelength synthesis imaging

While early VLBI, with its poorly calibrated phases, confronted difficulties very similar to optical aperture synthesis, we thought it would be interesting to compare optical long baseline interferometry with the millimeter one. mm-interferometry development offers an interesting operational parallel to what could be the future of optical interferometry.

Interferometry and aperture synthesis in the radio domain has been routinely achieved since the 1970s. The last 20 years have witnessed maturation in the millimeter domain as well, from the construction of large facilities such as the IRAM Plateau de Bure interferometer (six 15-m antennas, Guilloteau et al, 1992) to the Atacama Large Millimeter/submillimeter Array (ALMA, sixty-four 12-m antennas). Compared to the infrared domain, two major differences make millimeter interferometry easier to implement: (1) the coherence time of the atmosphere is longer, making it possible to reference the phase of the visibility to avoid relying on phase closure only, and (2) the millimeter receivers are directly sensitive to the incoming electric field, which is then down-converted to a frequency that can be processed with electronic equipments; as a consequence, the delay between two antennas can be corrected for after detection of each signal (before any interference) and the signal can be amplified to allow to combine many baselines simultaneously. Unlike in optical interferometry the phase calibration can be done by observing, non simultaneously, a point-source calibrator (within a much larger isoplanatic patch) within one coherence time. Therefore the complex visibilities, including both amplitudes and phases, can be *directly* computed. Images are then obtained by Fourier transforming the visibilities, and a deconvolution is later applied to correct for the artifacts introduced by the (u, v) plane sampling. Numerous examples of scientific results obtained with millimeter or submillimeter interferometry can be found in the literature (e.g. the special edition of *Astronomy and Astrophysics*, volume 468, 2007).

To measure the source visibility on long (larger than a few hundreds meters) baselines, special techniques must be deployed in order to correct for the atmospheric phase errors. These have to be tracked on timescales of ~ 1 second and water vapor radiometers have proved to yield very efficient corrections by estimating the atmospheric contribution to the phase error (water content). This cophasing process is much more painful in the optical domain where fringe-trackers must actually form the fringes in order to maintain the global wavefront as planar as possible (see e.g. Blind et al, 2011a). In order to obtain the best possible images, a special attention has then to be paid to the (u, v) plane coverage that is obtained in such millimeter observations. Indeed, the poor sampling of the (u, v) plane has been identified as one of the major limitations of the imaging process: the point-spread-function (PSF) of the synthesized instrument (the so-called *dirty beam*) is the Fourier Transform of the (u, v) coverage and may thus include strong sidelobes if the (u, v) sampling is poor, making the astronomical interpretation of the resulting images quite difficult. Although this can be partly corrected by the deconvolution process (CLEAN being the most widely algorithm used), obtaining directly a high-quality image is a central goal of the current instruments design and operations. The Plateau de Bure interferometer configurations have been optimized for that purpose (Karastergiou et al, 2006). The positions of the 64 ALMA antennas have also been optimized (ALMA memo #400), the large number of antennas making it possible to achieve almost perfect beam shapes. In such optimization, the goal is to obtain a Gaussian distribution in the (u, v) plane (which means higher weights on the short baselines), which results in a Gaussian PSF. The behavior of a single-dish telescope with Gaussian beam taper is thus reproduced as accurately as possible.

6.3 Improving image reconstruction

6.3.1 What is a good image reconstruction?

In this work, we wondered whether a reconstruction is a good representation of the model. Although visual inspection can do a good job, it is difficult to go further. It is useful to compare different results from different algorithms like in the Beauty Contests (Lawson et al, 2004, 2006; Cotton et al, 2008), but not really useful when assessing the quality of the image reconstruction by itself. Developing tools to compare relative positions or relative fluxes of the image features appears to be quite important but it is beyond the scope of this work. A systematic testing of image reconstruction “fidelity”, such as the one mentioned in Appendix B is an essential step to build the trust in image reconstruction. The reader is referred to Renard et al (2011) for a first attempt to test systematically the quality of image reconstruction.

The answer to the question of whether model fitting should be performed at the same time is certainly positive since this is the only way to deduce the quantitative parameters of the models. However, image reconstruction helps to recognize the general structure of the image which can be quite complex as illustrated in the supergiant and AGN cases. The modeler is then guided in his work by the general architecture revealed by the reconstructed image.

6.3.2 Improving current facilities

For this work, we used expected features of interferometers and instruments either in existence or under active development. In these cases, an ideal observing sequence is often impossible due to technical limits: finite range of delay lines, telescope shadowing, bad telescope tracking near zenith, etc. Indeed, to optimally use VLTI and CHARA, we must identify the current limitations of instruments at VLTI and CHARA.

VLTI. Some general remarks concerning image reconstruction at VLTI can be drawn: (i) so far simple objects are the most commonly imaged: binaries, simple circumstellar environments, or images with small field-of-view (perhaps 5x5 pixels at maximum); (ii) the main results have been obtained in visitor-mode with at least three configurations of 3 ATs; (iii) a sampling speed of the (u, v) plane at ≈ 25 min per calibrated observation has been shown to be sufficient; (iv) the poor quality of the calibrated visibilities is an important limitation leading to poor dynamic range; (v) the impossibility to track on resolved fringes ($< 10\%$) with the VLTI fringe tracking instrument FINITO is a limitation for imaging stellar surfaces; (vi) the observations are limited in hour angle because of the delay line stroke reducing the possible (u, v) coverage; (vii) finally all existing data sets suffer so far from an important hole in the (u, v) plane due to the current limitations in baseline configuration. In the coming years, the VLTI will improve imaging by prioritizing improved data quality as well as an increase of the number of offered interferometric baselines. Background work is on-going, focusing on several open questions (such as the trade-off between maximum baseline length, (u, v) plane density and sky-coverage).

CHARA. The fixed locations of the CHARA telescopes mean that the array can only image objects of a certain size range. For near-infrared, the ideal range for imaging is between 1.5 and 3.5 milli-arcseconds, since this allows all the 15 baselines of CHARA to make a useful contribution to the image reconstruction. If an object is smaller than this, then there is not enough resolution; if the object is bigger, then most of the short baselines are sampling beyond the first null and this means too much information is missing to reliably

invert the Fourier data. One way to improve imaging on CHARA substantially would be to add a telescope to the center of the array⁸ to introduce more small baselines and to aid the baseline bootstrapping. A simpler short-term solution to improving CHARA imaging is to use all 6 telescopes simultaneously with new combiners⁹.

6.4 How to obtain high-quality images

For future facilities, either new interferometers like MROI or new instruments on existing facilities, it is important to identify the most important criteria for high-quality imaging. The main practical limitations are related to the complexity, dynamic range, and magnitude of the source to be imaged.

As pointed out in Sect. 6.2, as in the radio domain the dominant source of artifacts is an inadequate (u, v) sampling. The causes may come from the number of positions of the telescopes (see the discussions above about current limitations at VLTI and CHARA), and the reduced stroke of the delay lines preventing full observation of the source through the sky. Most specialists agree that this is the major issue by a large margin. In our simulations, the (u, v) coverage does not seem to be a limitation, but we have been quite generous in (u, v) points. Experience with the MIRC/CHARA instrument shows that snapshot coverage with only 4 telescopes has proven adequate for imaging objects such as stars with simple spots and resolved binaries if they are of the "right" size. However, more complicated objects such as multiple components objects, crowded stellar fields or heavily spotted stars need more (u, v) coverage. In addition to that, short-baseline (u, v) sampling is an essential part when observing extended objects (such as the evolved star case (see also Monnier et al, 2004)). Diffraction-limited imaging with a conventional single-pupil telescope, or, preferably single dish aperture masking, like in millimeter-wave interferometry, might be an efficient way to cover that issue for relatively compact objects.

How many telescopes are needed? Millimeter-wave interferometers have found that 6-7 telescopes are adequate for many imaging applications and experienced observers with the CHARA/MIRC instrument are coming to similar conclusions. In the optical domain there is one crucial point that has to be integrated in this discussion: the ability to cophase the array. The so-called "fringe-trackers" of future generation instruments will have to cope with the difficulty that highly detailed images require high spatial frequency measurements. This translates into a strong requirement on these cophasing instruments and on the array configuration: they need to be able to maintain the array phasing while measuring small visibilities. While this consideration was integrated in the design of NPOI (e.g. Armstrong et al, 1998a) and MROI through the use of array configurations allowing for baseline bootstrapping, this was not the case for VLTI. The ability to re-configure telescope locations will be another key to making images of high spatial dynamic range, although many interesting objects such as spotted rotating stars and binary systems generally change in time too quickly to make re-configuring practical to schedule.

Spectral dispersion has been quite successful to increase the (u, v) coverage by wavelength synthesis. Line maps have been obtained at NPOI for a long time (e.g. Schmitt et al, 2009) while this has only become possible recently at VLTI with the advent of the AMBER high resolution spectroscopy capability Millour et al (2011). Observations in an absorption

⁸ This addition is feasible since there is space on the mountain top for the telescope and space in the lab for the delay line.

⁹ The MIRC 6-T upgrade was successfully completed in summer 2012.

line and in the continuum probe different atmospheric depths and thus layers at different temperatures. Such photosphere observations provide important information on the wavelength dependence of limb darkening and therefore possibly a strong constraint to the supergiant case (and all stellar-surface imaging). Another interesting application is the comparison between a central star emitting in the continuum and its surrounding hot line-emitting disk. Specific algorithms could be developed to image simultaneously all channels within a line (e.g. taking into account the fact that a smooth transition from one channel to the next one is expected) although this has never been done in the millimeter wave domain where each channel is imaged separately, most probably because the (u, v) coverage is sufficient for such mappings.

Finally, flux sensitivity and measurement accuracies appear to impose a quite stringent limitation. The dynamic range DN is not only a direct function of the number n of (u, v) points but also of the errors on each measurements δV and $\delta\phi$ as pointed out by Baldwin and Haniff (2002) who propose a rule-of-thumb estimator: $DN = \sqrt{n}/[(\delta V/V)^2 + (\delta\phi)^2]$. This ideal metric relies on the independence of the measurements whose calibration should remain uncorrelated. Instruments should therefore be conceived to allow for precisely calibrated measurements.

The temporal fluctuations of the sources might be a severe limitation especially with interferometers having a limited number of telescope combinations. For example, the timescale of convection is crucial to constrain the simulations of red-supergiant stars. We probably need a time series of observations (at least 4-5 different epochs) about 1-2 months apart in the H and K bands where only small differences are predicted and at maximum 1 month apart in the optical where things change faster. Increasingly, we do find our prime targets changing on timescales of days or even hours and imaging snapshots will require as many simultaneous measurements as possible¹⁰.

7 Conclusions

We have reviewed past and present efforts to generate aperture synthesis maps from optical long baseline interferometers showing the tremendous progresses obtained since 1996. We have presented in this paper end-to-end simulations of 4 different astrophysical cases relevant for image reconstruction with optical interferometers. The purpose of these simulations was to assess if reconstructed images would be faithful enough to be trusted when interpreting the results and to identify ways to increase the quality of the reconstructed images. This was not a trivial process and it required the contribution of a large range of competences from astrophysicists able to create sensible images of the objects, interferometry experts to mock realistic data, and specialists of image reconstruction to reach the best reconstructed images. We addressed four different topics of interest for optical long-baseline interferometry and found the following results:

- Detection of planet signatures in disk structures like shadows are challenged by dynamic range and might be out of reach of current optical interferometry facilities. However other larger-scale structures, with lower contrasts such as disk gravity waves, gaps, hot accreting bubbles around a protoplanet etc. might be revealed. Future efforts in that direction should address both instrumental issues (precision and accuracy of measurements, data reduction) and image-reconstruction dynamic range limits.

¹⁰ A warning to researchers that believe building up many 3-telescope observations is the best approach: it takes 20x longer to build up full closure phase coverage one triplet at a time for a 6-telescope interferometer compared to schemes which measure all baselines!.

- Interferometric imaging allows sizes of convection cells and the contrast of the surface intensity to be measured and allows us to better understand the photosphere and dynamics of evolved massive stars. These results are crucial for understanding their unknown mass loss mechanism that contributes heavily to the chemical enrichment of the Galaxy. The complex structure requires a rich (u, v) plane sampling and therefore the combination of the highest possible number of telescopes.
- The capabilities offered by current interferometers make it possible to reveal asymmetries in the molecular layers around evolved stars. Further imaging of molecular layers appearing in spectral lines is the path to understand these dust and molecule factories of the Galaxy.
- Our simulations show that unraveling the clumpy structure of the dusty torus obscuration region in AGN is within reach and will certainly be a necessary step to progress in the understanding of the AGN unified scheme.

In general, we found that image-reconstruction techniques have been successful at retrieving global morphologies of all our objects. Their current limitations lie (i) in their ability to match exact intensities and (ii) to detect highly contrasted features.

The (u, v) coverage is of crucial and primary importance and therefore we look forward to results from the 6-telescope mode of CHARA/MIRC, the implementation of at least 6 (up to 8) telescopes at the VLTI with a fully operational set of delay lines, and the construction of MROI with full capacity. We also recall the importance of imaging instruments (Matisse, Gravity, VSI at VLTI, MIRC and MIRC6T at CHARA). The spectral resolution is an asset whose full exploitation has only started to be fully exploited. Of course, like in millimeter astronomy, the future of interferometry has to be prepared and will probably aim at a facility similar to the *Very Large Array (VLA)* or ALMA.

Our study also shows that, in the context of image reconstruction, the tools have reached a certain level of maturity to produce on-the-fly results and with a reliability and reproducibility that allows productive results and discussion. Optimization of the “*theory* → *models* → *simulated observations* → *reconstructed images*” cycle is never finished, but a first level of quantitative analysis shows that optical interferometry is capable of producing meaningful images. We have now tools to improve the comprehension of astrophysical phenomena and to reach ambitious research topics.

We believe that imaging interferometry will provide to the broad astronomical community a new window to the universe if we are able to gather resources (expertise, manpower and relatively limited investments).

Acknowledgements We are very grateful to A. Quirrenbach, the referee, for his in-depth reading and his many suggestions that helped improve the article. This work is the result of a workshop on *Interferometry Imaging* held in Château de Goutelas from 26 May to 29 May 2009 and organized by F. Malbet and J.-P. Berger following an idea of J.-L. Monin. We would like to thank the members of the *Science Organizing Committee* O. Chesneau, T. Driebe, A. Marconi, J. Monnier, B. Plez, L. Testi, S. Wolf and J. Young, as well as the *Local Organizing Committee*. This workshop has been possible thanks to the financial participation of the *Laboratoire d’Astrophysique de Grenoble (LAOG)*, of the *Programme National of Physique Stellaire (PNPS)* from CNRS, the *Jean-Marie Mariotti Center (JMMC)* and the *Université Joseph Fourier*. The web page for the workshop is at <http://wii09.obs.ujf-grenoble.fr>. M. Elitzur acknowledges the support of NSF (AST-0807417) and NASA (SSC-40095). S. Hönl acknowledges support by DFG. T.V. acknowledges support from the Fund for Scientific Research, Flanders as Postdoctoral Fellow”. ”B.F. acknowledges financial support from ANR and the PNPS of CNRS/INSU, France.” This research has made use of the Jean-Marie

Mariotti Center SearchCal service ¹¹. We have made use of the SAO/NASA Astrophysics Data System. Figures were generated using the free Yorick software, under BSD license ¹².

A Noise model for ASPRO simulations

This Appendix is aimed at describing the noise model used in ASPRO for creating the simulations used in this paper (see Sect. 5.2).

The noise model is based on a general scheme valid for spatially filtered recombiners where the detection of fringes is made on a detector with “pixels”. This scheme is valid for image-plane recombination, with fringes covering a surface of a pixel camera, and for pupil recombination where fringes are obtained on a few pixels detector by scanning in optical path difference.

The flux $\overline{N}_{\text{tot}}$ from the object of magnitude m_b in a given bandwidth $\Delta\lambda$ of a photometric band b is collected by N_{tel} telescopes of diameter D , transmitted with some instrumental transmission T_{inst} , and injected with some Strehl factor s due to incomplete correction of wavefront aberrations due to seeing into a spatial filter like an optical single mode fiber for example, during a time t_{int} . Thus:

$$\overline{N}_{\text{tot}} = \eta F_0 10^{-0.4m_b} T_{\text{inst}} N_{\text{tel}} s \frac{\pi D^2}{4} \Delta\lambda, \quad (5)$$

where F_0 is the zero-magnitude flux in band b , expressed in $\text{ph s}^{-1} \text{m}^{-2} \mu\text{m}^{-1}$ transmitted through the atmosphere with an absorption η .

This flux is divided between the photometric flux and interferometric flux with a branching value b_i , where b_i equals 1 for recombiners which do not have simultaneous flux monitoring.

The N_{tel} photometric fluxes $\overline{N}_p = (1 - b_i) \overline{N}_{\text{tot}} / N_{\text{tel}}$ are distributed on N_{pix} pixels. The interferometric flux $\overline{N}_i = b_i \overline{N}_{\text{tot}} / N_{\text{tel}}$ consists in $N_f = N_{\text{tel}} (N_{\text{tel}} - 1) / 2$ fringes that cover N_{pix}^i pixels. There are thus $N_{\text{ppf}} = N_{\text{pix}}^i / N_f$ pixels per fringe.

These fringes code the intrinsic visibility $V(u, v, \lambda)$ degraded by the interferometer instrumental contrast and the atmosphere (through the jitter associated with the temporal coherence of the seeing). $V(u, v, \lambda)$ and the derived interferometric observables are thus affected by the sum of the variance of the flux used to code the corresponding fringe in the interferometric flux and of the associated two photometric fluxes. For example, since the squared visibility estimator of a correlated flux F_c^{ij} measured alongside with photometries F_i and F_j is $V^2 = \frac{1}{4} \langle |F_c^{ij}|^2 \rangle / \langle F_i F_j \rangle$, the associated variance is

$$\sigma^2(V^2) = \overline{N}_i V(u, v, \lambda) + N_{\text{ppf}} \sigma_{\text{det}}^2 + 2 \left(\overline{N}_p + N_{\text{pix}}^p \sigma_{\text{det}}^2 \right), \quad (6)$$

where σ_{det} is the readout noise of the detector.

The noise model used in ASPRO takes also into account the possibility of increasing the integration time to keep observations in a photon-dominated regime, when a fringe tracker is present.

Finally, no detailed calibration error was computed. We took instead an additional visibility and closure phase threshold error set to 0.002 in visibility, and 0.1 degree in closure phase.

B Computing fidelities

Testing image reconstruction software is out of scope of this paper. In this Appendix, we follow the approach described in ALMA Memo 398 (F. Gueth private communication) to evaluate the quality of the reconstructed images presented in this paper. One of the possible methods to compare original (convolved to the interferometer resolution) and reconstructed image is to compute the *fidelity* of the image. This can be done either in the direct image plane or in the spatial frequency (u, v) plane. Such a pixel to pixel comparison requires subpixel alignment to limit the effect of sharp transitions.

In the image plane this fidelity can be expressed as

$$\mathcal{F}(x, y) = \frac{\text{abs}(\text{Model}(x, y))}{\max(\text{Diff}(x, y), \text{Threshold})}, \quad (7)$$

¹¹ Available at <http://www.jmmc.fr/aspro>

¹² Available at <http://www.maumae.net/yorick/doc/index.php>

Table 6 For a given fraction of the brightest pixels (col 1) the corresponding number of pixels, median and average fidelity is given for each object.

Fraction of brightest pixels	Supergiant (100 × 100 pixels)			Evolved Star (200 × 200 pixels)			AGN (200 × 200 pixels)		
	N_{pixel}	Med	Avg	N_{pixel}	Med	Avg	N_{pixel}	Med	Avg
0.3%	30	2.9	3.2	119	13.7	30.7	122	1.4	2.9
1%	100	3.6	4.8	398	4.4	14.0	408	1.4	4.5
10%	1000	5.7	11.5	3980	0.0	1.4	4080	1.5	4.5

where $Model(x, y)$ describes the object “true” brightness distribution and

$$Diff(x, y) = Model(x, y) - Reconstructed(x - \Delta x, y - \Delta y) \quad (8)$$

describes the difference between the model and the reconstructed image shifted by the offset $(\Delta x, \Delta y)$ to have the images centered. For a proper comparison images are normalized to the total intensity contain in the image. $Threshold$ is defined here as $0.7 \text{ rms}[Diff(x, y)]$ which provides an estimation of the threshold noise of this difference. For example a pixel fidelity of 100 corresponds to a difference of 1% between the model and reconstructed image. We have computed such a fidelity for three of our objects: the supergiant, the evolved star and the active galactic nuclei. Figures 10 and 11 offer different ways to visualize fidelity. The first row shows the cumulated average fidelity over the image for the three different objects. The second row displays the original model image filtered by fidelity level, i.e. only the pixels with fidelity above a certain level are displayed. Finally Table 6 shows the average fidelity of the pixels whose intensity is above a certain fraction of the total image intensity.

References

- Adams FC, Lada CJ, Shu FH (1987) Spectral evolution of young stellar objects. *ApJ*312:788–806, DOI 10.1086/164924
- Allende Prieto C, Lambert DL, Asplund M (2001) The Forbidden Abundance of Oxygen in the Sun. *ApJ*556:L63–L66, DOI 10.1086/322874, [arXiv:astro-ph/0106360](https://arxiv.org/abs/astro-ph/0106360)
- Antonucci R (1993) Unified models for active galactic nuclei and quasars. *ARA&A*31:473–521, DOI 10.1146/annurev.aa.31.090193.002353
- Antonucci R (2002) Polarization insights for active galactic nuclei. In: Trujillo-Bueno J, Moreno-Inertis F, Sánchez F (eds) *Astrophysical Spectropolarimetry*, pp 151–175
- Armstrong JT, Mozurkewich D, Pauls TA, Hajian AR (1998a) Bootstrapping the NPOI: keeping long baselines in phase by tracking fringes on short baselines. In: R D Reasenberg (ed) *Society of Photo-Optical Instrumentation Engineers (SPIE) Conference Series*, Society of Photo-Optical Instrumentation Engineers (SPIE) Conference Series, vol 3350, pp 461–466
- Armstrong JT, Mozurkewich D, Rickard LJ, Hutter DJ, Benson JA, Bowers PF, Elias NM II, Hummel CA, Johnston KJ, Buscher DF, Clark JH III, Ha L, Ling LC, White NM, Simon RS (1998b) The Navy Prototype Optical Interferometer. *ApJ*496:550, DOI 10.1086/305365
- Baldwin JE, Haniff CA (2002) The application of interferometry to optical astronomical imaging. *Royal Society of London Philosophical Transactions Series A* 360:969
- Baldwin JE, Haniff CA, Mackay CD, Warner PJ (1986) Closure phase in high-resolution optical imaging. *Nature*320:595–597, DOI 10.1038/320595a0
- Baldwin JE, Beckett MG, Boysen RC, Burns D, Buscher DF, Cox GC, Haniff CA, Mackay CD, Nightingale NS, Rogers J, Scheuer PAG, Scott TR, Tuthill PG, Warner PJ, Wilson DMA, Wilson RW (1996) The first images from an optical aperture synthesis array: mapping of Capella with COAST at two epochs. *A&A*306:L13
- Baron F, Young JS (2008) Image reconstruction at Cambridge University. *SPIE* 7013:E121, DOI 10.1117/12.789115
- Bate MR, Lubow SH, Ogilvie GI, Miller KA (2003) Three-dimensional calculations of high- and low-mass planets embedded in protoplanetary discs. *MNRAS*341:213–229, DOI 10.1046/j.1365-8711.2003.06406.x, [arXiv:astro-ph/0301154](https://arxiv.org/abs/astro-ph/0301154)
- Beckwith SVW, Sargent AI, Chini RS, Güsten R (1990) A survey for circumstellar disks around young stellar objects. *AJ*99:924–945, DOI 10.1086/115385

- Benisty M, Tatulli E, Ménard F, Swain MR (2010) The complex structure of the disk around HD 100546. The inner few astronomical units. *A&A*511:A75, DOI 10.1051/0004-6361/200913590, 1001.2491
- Benisty M, Renard S, Natta A, Berger JP, Massi F, Malbet F, Garcia PJV, Isella A, Mérand A, Monin JL, Testi L, Thiébaud E, Vannier M, Weigelt G (2011) A low optical depth region in the inner disk of the Herbig Ae star HR 5999. *A&A*531:A84, DOI 10.1051/0004-6361/201016091, 1106.4150
- Benson JA, Hutter DJ, Elias NM II, Bowers PF, Johnston KJ, Hajian AR, Armstrong JT, Mozurkewich D, Pauls TA, Rickard LJ, Hummel CA, White NM, Black D, Denison CS (1997) Multichannel optical aperture synthesis imaging of zeta1 URSAE majoris with the Navy prototype optical interferometer. *AJ*114:1221–1226, DOI 10.1086/118554
- Berger JP, Zins G, Lazareff B, Lebouquin JB, Jocu L, Kern P, Millan-Gabet R, Traub W, Haguenaer P, Absil O, Augereau JC, Benisty M, Blind N, Bonfils X, Delboulbe A, Feautrier P, Germain M, Gillier D, Gitton P, Kiekebusch M, Knudstrup J, Lizon JL, Magnard Y, Malbet F, Maurel D, Menard F, Micallef M, Michaud L, Morel S, Moulin T, Popovic D, Perraut K, Rabou P, Rochat S, Roussel F, Roux A, Stadler E, Tatulli E (2010) PIONIER: a visitor instrument for VLTI. In: Society of Photo-Optical Instrumentation Engineers (SPIE) Conference Series, Society of Photo-Optical Instrumentation Engineers (SPIE) Conference Series, vol 7734, DOI 10.1117/12.858647, 1008.5352
- Blind N, Absil O, Le Bouquin JB, Berger JP, Chelli A (2011a) Optimized fringe sensors for the VLTI next generation instruments. *A&A*530:A121, DOI 10.1051/0004-6361/201016222, 1104.1934
- Blind N, Boffin HMJ, Berger JP, Le Bouquin JB, Mérand A, Lazareff B, Zins G (2011b) An incisive look at the symbiotic star γ ASTROBJ $_{\zeta}$ SS Leporis $_{\zeta}$ /ASTROBJ $_{\zeta}$. Milli-arcsecond imaging with PIONIER/VLTI. *A&A*536:A55, DOI 10.1051/0004-6361/201118036, 1112.1514
- Buscher DF (1994) Direct maximum-entropy image reconstruction from the bispectrum. In: Robertson JG, Tango WJ (eds) Very High Angular Resolution Imaging, IAU Symposium, vol 158, p 91
- Buscher DF, Baldwin JE, Warner PJ, Haniff CA (1990) Detection of a bright feature on the surface of Betelgeuse. *MNRAS*245:7–11
- Caffau E, Ludwig HG, Steffen M, Ayres TR, Bonifacio P, Cayrel R, Freytag B, Plez B (2008) The photospheric solar oxygen project. I. Abundance analysis of atomic lines and influence of atmospheric models. *A&A*488:1031–1046, DOI 10.1051/0004-6361:200809885, 0805.4398
- Chiavassa A, Plez B, Josselin E, Freytag B (2009) Radiative hydrodynamics simulations of red supergiant stars. I. interpretation of interferometric observations. *A&A*506:1351–1365, DOI 10.1051/0004-6361/200911780, 0907.1860
- Chiavassa A, Haubois X, Young JS, Plez B, Josselin E, Perrin G, Freytag B (2010) Radiative hydrodynamics simulations of red supergiant stars. II. Simulations of convection on Betelgeuse match interferometric observations. *A&A*515:A12, DOI 10.1051/0004-6361/200913907, 1003.1407
- Cornwell TJ, Wilkinson PN (1981) A new method for making maps with unstable radio interferometers. *MNRAS*196:1067–1086
- Cotton W, Monnier J, Baron F, Hofmann K, Kraus S, Weigelt G, Rengaswamy S, Thiébaud E, Lawson P, Jaffe W, Hummel C, Pauls T, Schmitt H, Tuthill P, Young J (2008) 2008 imaging beauty contest. *SPIE* 7013, DOI 10.1117/12.788903
- Creech-Eakman MJ, Romero V, Westpfahl D, Cormier C, Haniff C, Buscher D, Bakker E, Berger L, Block E, Coleman T, Festler P, Jurgenson C, King R, Klingle-Smith D, McCord K, Olivares A, Parameswariah C, Payne I, Paz T, Ryan E, Salcido C, Santoro F, Selina R, Shtromberg A, Steenson J, Baron F, Boysen R, Coyne J, Fisher M, Seneta E, Sun X, Thureau N, Wilson D, Young J (2008) Magdalena Ridge Observatory Interferometer: progress toward first light. *SPIE* 7013:26, DOI 10.1117/12.789859
- Crida A, Morbidelli A (2007) Cavity opening by a giant planet in a protoplanetary disc and effects on planetary migration. *MNRAS*377:1324–1336, DOI 10.1111/j.1365-2966.2007.11704.x, arXiv:astro-ph/0703151
- D'Alessio P, Canto J, Calvet N, Lizano S (1998) Accretion Disks around Young Objects. I. The Detailed Vertical Structure. *ApJ*500:411
- Delplancke F (2008) The PRIMA facility phase-referenced imaging and micro-arcsecond astrometry. *New A Rev.*52:199–207, DOI 10.1016/j.newar.2008.04.016
- Delplancke F, Derie F, Lévyque S, Ménardi S, Abuter R, Andolfato L, Ballester P, de Jong J, Di Lieto N, Duhoux P, Frahm R, Gitton P, Glindemann A, Palsa R, Puech F, Sahlmann J, Schuhler N, Duc TP, Valat B, Wallander A (2006) PRIMA for the VLTI: a status report. *SPIE* 6268:E27, DOI 10.1117/12.660395
- Dravins D, Lindegren L, Nordlund A (1981) Solar granulation - Influence of convection on spectral line asymmetries and wavelength shifts. *A&A*96:345–364
- Dutrey A, Guilloteau S, Duvert G, Prato L, Simon M, Schuster K, Ménard F (1996) Dust and gas distribution around T Tauri stars in Taurus-Auriga. I. Interferometric 2.7mm continuum and ^{13}CO J=1-0 observations. *A&A*309:493–504
- Duvert G, Bério P, Malbet F (2002) ASPRO, a software to prepare observations with optical interferometers.

- SPIE 4844:295, DOI 10.1117/12.460600
- Eisenhauer F, Perrin G, Brandner W, Straubmeier C, Richichi A, Gillessen S, Berger JP, Hippler S, Eckart A, Schöller M, Rabien S, Cassaing F, Lenzen R, Thiel M, Clénet Y, Ramos JR, Kellner S, Fédou P, Baumeister H, Hofmann R, Gendron E, Boehm A, Bartko H, Haubois X, Klein R, Dodds-Eden K, Houairi K, Hormuth F, Gräter A, Jocou L, Naranjo V, Genzel R, Kervella P, Henning T, Hamaus N, Lacour S, Neumann U, Haug M, Malbet F, Laun W, Kolmeder J, Paumard T, Rohloff R, Pfuhl O, Perraut K, Ziegleder J, Rouan D, Rousset G (2008) GRAVITY: getting to the event horizon of Sgr A*. SPIE 7013:E69, DOI 10.1117/12.788407
- Eisner JA, Graham JR, Akeson RL, Ligon ER, Colavita MM, Basri G, Summers K, Ragland S, Booth A (2007) Stellar and Molecular Radii of a Mira Star: First Observations with the Keck Interferometer Grism. *ApJ*654:L77–L80, DOI 10.1086/510717, arXiv:astro-ph/0611312
- Elitzur M (2008) The toroidal obscuration of active galactic nuclei. *New Astronomy Review* 52:274–288, DOI 10.1016/j.newar.2008.06.010, 0805.3699
- Fedele D, Wittkowski M, Paresce F, Scholz M, Wood PR, Cirotti S (2005) The K-band intensity profile of R Leonis probed by VLTI/VINCI. *A&A*431:1019–1026, DOI 10.1051/0004-6361:20042013, arXiv:astro-ph/0411133
- Freytag B, Höfner S (2008) Three-dimensional simulations of the atmosphere of an AGB star. *A&A*483:571–583, DOI 10.1051/0004-6361:20078096
- Freytag B, Ludwig HG, Steffen M (1996) Hydrodynamical models of stellar convection. The role of overshoot in DA white dwarfs, A-type stars, and the Sun. *A&A*313:497–516
- Freytag B, Steffen M, Dorch B (2002) Spots on the surface of Betelgeuse – Results from new 3D stellar convection models. *Astronomische Nachrichten* 323:213–219
- Freytag B, Allard F, Ludwig HG, Homeier D, Steffen M (2008) Models of surface convection and dust clouds in brown dwarfs. *Physica Scripta Volume T* 133(1):014,005, DOI 10.1088/0031-8949/2008/T133/014005
- Glindeemann A (2011) Principles of Stellar Interferometry
- Goodman JW (1985) Statistical Optics
- Gray DF (2008) Mass Motions in the Photosphere of Betelgeuse. *AJ*135:1450–1458, DOI 10.1088/0004-6256/135/4/1450
- Guilloteau S, Delannoy J, Downes D, Greve A, Guelin M, Lucas R, Morris D, Radford SJE, Wink J, Cernicharo J, Forveille T, Garcia-Burillo S, Neri R, Blondel J, Perrigourad A, Plathner D, Torres M (1992) The IRAM interferometer on Plateau de Bure. *A&A*262:624–633
- Gull SF, Skilling J (1984) The Maximum Entropy Method. In: J A Roberts (ed) *Indirect Imaging. Measurement and Processing for Indirect Imaging*, p 267
- Gustafsson B, Bell RA, Eriksson K, Nordlund A (1975) A grid of model atmospheres for metal-deficient giant stars. I. *A&A*42:407–432
- Haguenauer P, Abuter R, Alonso J, Argomedo J, Bauvir B, Blanchard G, Bonnet H, Brilliant S, Cantzler M, Derie F, Delplancke F, Di Lieto N, Dupuy C, Durand Y, Gitton P, Gilli B, Glindeemann A, Guniat S, Guisard S, Haddad N, Hudepohl G, Hummel C, Jesuran N, Kaufer A, Koehler B, Le Bouquin JB, Lévêque S, Lidman C, Mardones P, Ménardi S, Morel S, Percheron I, Petr-Gotzens M, Phan Duc T, Puech F, Ramirez A, Rantakyro F, Richichi A, Rivinius T, Sahlmann J, Sandrock S, Schöller M, Schuhler N, Somboli F, Stefl S, Tapia M, Van Belle G, Wallander A, Wehner S, Wittkowski M (2008) The Very Large Telescope Interferometer: an update. SPIE 7013:E11, DOI 10.1117/12.788209
- Haniff C (2007) Ground-based optical interferometry: A practical primer. *New Astronomy Review* 51:583–596, DOI 10.1016/j.newar.2007.06.004
- Haniff CA, Mackay CD, Titterton DJ, Sivia D, Baldwin JE (1987) The first images from optical aperture synthesis. *Nature*328:694–696, DOI 10.1038/328694a0
- Haubois X, Perrin G, Lacour S, Verhoelst T, Meimon S, Mugnier L, Thiébaud E, Berger JP, Ridgway ST, Monnier JD, Millan-Gabet R, Traub W (2009) Imaging the spotty surface of μ AS-TROBJ_iBetelgeuse/ μ ASTROBJ_i in the H band. *A&A*508:923–932, DOI 10.1051/0004-6361/200912927, 0910.4167
- Hofmann KH, Weigelt G (1993) Iterative image reconstruction from the bispectrum. *A&A*278:328–339
- Hofmann KH, Kraus S, Lopez B, Weigelt G, Wolf S (2006) Aperture synthesis image reconstruction study for the mid-infrared VLTI imager MATISSE. SPIE 6268:E112, DOI 10.1117/12.671678
- Höfner S, Gautschi-Loidl R, Aringer B, Jørgensen UG (2003) Dynamic model atmospheres of AGB stars. III. Effects of frequency-dependent radiative transfer. *A&A*399:589–601, DOI 10.1051/0004-6361:20021757
- Högbom JA (1974) Aperture Synthesis with a Non-Regular Distribution of Interferometer Baselines. *A&AS*15:417
- Hönig SF, Kishimoto M (2010) The dusty heart of nearby active galaxies. II. From clumpy torus models to physical properties of dust around AGN. *A&A*523:A27, DOI 10.1051/0004-6361/200912676, 0909.4539
- Hönig SF, Beckert T, Ohnaka K, Weigelt G (2006) Radiative transfer modeling of three-dimensional clumpy

- AGN tori and its application to NGC 1068. *A&A*452:459–471, DOI 10.1051/0004-6361/20054622, arXiv:astro-ph/0602494
- Hönig SF, Prieto MA, Beckert T (2008) High-spatial resolution SED of NGC 1068 from near-IR to radio. Disentangling the thermal and non-thermal contributions. *A&A*485:33–39, DOI 10.1051/0004-6361:200809606, 0804.0236
- Hutter DJ, Benson JA, Buschmann T, DiVittorio M, Zavala RT, Johnston KJ, Armstrong JT, Hindsley RB, Schmitt HR, Clark JH III, Restaino SR, Tycner C, Jorgensen AM, Davis S (2008) NPOI: recent progress and future prospects. In: Society of Photo-Optical Instrumentation Engineers (SPIE) Conference Series, Society of Photo-Optical Instrumentation Engineers (SPIE) Conference Series, vol 7013, DOI 10.1117/12.787486
- Ireland MJ, Scholz M, Wood PR (2004) On the observability of geometric pulsation of M-type Mira variables. *MNRAS*352:318–324, DOI 10.1111/j.1365-2966.2004.07928.x
- Ireland MJ, Monnier JD, Thureau N (2006) Monte-Carlo imaging for optical interferometry. *SPIE* 6268:E58, DOI 10.1117/12.670940
- Jaffe W, Meisenheimer K, Röttgering HJA, Leinert C, Richichi A, Chesneau O, Fraix-Burnet D, Glazenberg-Kluttig A, Granato GL, Graser U, Heijligers B, Köhler R, Malbet F, Miley GK, Paresce F, Pel JW, Perrin G, Przygodda F, Schoeller M, Sol H, Waters LBFM, Weigelt G, Wöillez J, de Zeeuw PT (2004) The central dusty torus in the active nucleus of NGC 1068. *Nature*429:47–49, DOI 10.1038/nature02531
- Jang-Condell H (2008) Planet Shadows in Protoplanetary Disks. I. Temperature Perturbations. *ApJ*679:797–812, DOI 10.1086/533583, arXiv:0801.4561
- Jang-Condell H (2009) Planet Shadows in Protoplanetary Disks. II. Observable Signatures. *ApJ*700:820–831, DOI 10.1088/0004-637X/700/1/820, 0906.1375
- Jennison RC (1958) A phase sensitive interferometer technique for the measurement of the Fourier transforms of spatial brightness distributions of small angular extent. *MNRAS*118:276
- Josselin E, Plez B (2007) Atmospheric dynamics and the mass loss process in red supergiant stars. *A&A*469:671–680, DOI 10.1051/0004-6361/20066353, 0705.0266
- Karastergiou A, Neri R, Gurwell MA (2006) Adapting and Expanding Interferometric Arrays. *ApJS*164:552–558, DOI 10.1086/503630, arXiv:astro-ph/0602578
- Keller SC, Wood PR (2006) Bump Cepheids in the Magellanic Clouds: Metallicities, the Distances to the LMC and SMC, and the Pulsation-Evolution Mass Discrepancy. *ApJ*642:834–841, DOI 10.1086/501115, arXiv:astro-ph/0601225
- Kervella P, Verhoelst T, Ridgway ST, Perrin G, Lacour S, Cami J, Haubois X (2009) The close circumstellar environment of Betelgeuse. Adaptive optics spectro-imaging in the near-IR with VLT/NACO. *A&A*504:115–125, DOI 10.1051/0004-6361/200912521, 0907.1843
- Kishimoto M, Hönig SF, Antonucci R, Barvainis R, Kotani T, Tristram KRW, Weigelt G, Levin K (2011) The innermost dusty structure in active galactic nuclei as probed by the Keck interferometer. *A&A*527:A121, DOI 10.1051/0004-6361/201016054, 1012.5359
- Kloppenborg B, Stencel R, Monnier JD, Schaefer G, Zhao M, Baron F, McAlister H, Ten Brummelaar T, Che X, Farrington C, Pedretti E, Sallave-Goldfinger PJ, Sturmman J, Sturmman L, Thureau N, Turner N, Carroll SM (2010) Infrared images of the transiting disk in the ϵ Aurigae system. *Nature*464:870–872, DOI 10.1038/nature08968, 1004.2464
- Kraus S, Weigelt G, Balega YY, Docobo JA, Hofmann KH, Preibisch T, Schertl D, Tamazian VS, Driebe T, Ohnaka K, Petrov R, Schöller M, Smith M (2009) Tracing the young massive high-eccentricity binary system θ^1 Orionis C through periastron passage. *A&A*497:195–207, DOI 10.1051/0004-6361/200810368, 0902.0365
- Kraus S, Hofmann KH, Menten KM, Schertl D, Weigelt G, Wyrowski F, Meilland A, Perraut K, Petrov R, Robbe-Dubois S, Schilke P, Testi L (2010) A hot compact dust disk around a massive young stellar object. *Nature*466:339–342, DOI 10.1038/nature09174, 1007.5062
- Krolik JH, Begelman MC (1988) Molecular tori in Seyfert galaxies - Feeding the monster and hiding it. *ApJ*329:702–711, DOI 10.1086/166414
- Labeyrie A, Koechlin L, Bonneau D, Blazit A, Foy R (1977) Strong TiO-related variations in the diameters of Mira and R Leonis. *ApJ*218:L75–L78, DOI 10.1086/182579
- Lacour S, Meimon S, Thiébaud E, Perrin G, Verhoelst T, Pedretti E, Schuller PA, Mugnier L, Monnier J, Berger JP, Haubois X, Poncelet A, Le Besnerais G, Eriksson K, Millan-Gabet R, Ragland S, Lacasse M, Traub W (2008) The limb-darkened Arcturus: imaging with the IOTA/IONIC interferometer. *A&A*485:561–570, DOI 10.1051/0004-6361:200809611, 0804.0192
- Lacour S, Thiébaud E, Perrin G, Meimon S, Haubois X, Pedretti E, Ridgway ST, Monnier JD, Berger JP, Schuller PA, Woodruff H, Poncelet A, Le Coroller H, Millan-Gabet R, Lacasse M, Traub W (2009) The Pulsation of χ Cygni Imaged by Optical Interferometry: A Novel Technique to Derive Distance and Mass of Mira Stars. *ApJ*707:632–643, DOI 10.1088/0004-637X/707/1/632, 0910.3869

- Lawson PR (ed) (2000) *Principles of Long Baseline Stellar Interferometry*
- Lawson PR, Cotton WD, Hummel CA, Monnier JD, Zhao M, Young JS, Thorsteinsson H, Meimon SC, Mugnier LM, Le Besnerais G, Thiebaut EM, Tuthill PG (2004) An interferometry imaging beauty contest. *SPIE* 5491:886
- Lawson PR, Cotton WD, Hummel CA, Baron F, Young JS, Kraus S, Hofmann K, Weigelt GP, Ireland M, Monnier JD, Thiébaud E, Rengaswamy S, Chesneau O (2006) 2006 interferometry imaging beauty contest. *SPIE* 6268:E59, DOI 10.1117/12.670409
- Le Bouquin JB, Lacour S, Renard S, Thiébaud E, Merand A, Verhoelst T (2009) Pre-maximum spectro-imaging of the Mira star T Leporis with AMBER/VLTI. *A&A*496:L1–L4, DOI 10.1051/0004-6361/200811579, 0902.3698
- Le Bouquin JB, Berger JP, Lazareff B, Zins G, Haguenaer P, Jocu L, Kern P, Millan-Gabet R, Traub W, Absil O, Augereau JC, Benisty M, Blind N, Bonfils X, Bourget P, Delboulbe A, Feautrier P, Germain M, Gitton P, Gillier D, Kiekebusch M, Kluska J, Knudstrup J, Labeye P, Lizon JL, Monin JL, Magnard Y, Malbet F, Maurel D, Ménard F, Micallef M, Michaud L, Montagnier G, Morel S, Moulin T, Perraut K, Popovic D, Rabou P, Rochat S, Rojas C, Roussel F, Roux A, Stadler E, Steff S, Tatulli E, Ventura N (2011) PIONIER: a 4-telescope visitor instrument at VLTI. *A&A*535:A67, DOI 10.1051/0004-6361/201117586, 1109.1918
- Leinert C, Graser U, Waters LBFM, Perrin GS, Jaffe W, Lopez B, Przygodda F, Chesneau O, Schuller PA, Glazenberg-Kluttig AW, Laun W, Ligor S, Meisner JA, Wagner K, Bakker EJ, Cotton B, de Jong J, Mathar R, Neumann U, Storz C (2003) Ten-micron instrument MIDI: getting ready for observations on the VLTI. *SPIE* 4838:893
- Levesque EM, Massey P, Olsen KAG, Plez B, Josselin E, Maeder A, Meynet G (2005) The Effective Temperature Scale of Galactic Red Supergiants: Cool, but Not As Cool As We Thought. *ApJ*628:973–985, DOI 10.1086/430901, arXiv:astro-ph/0504337
- Lissauer JJ (1993) Planet formation. *ARA&A*31:129–174, DOI 10.1146/annurev.aa.31.090193.001021
- Lopez B, Antonelli P, Wolf S, Lagarde S, Jaffe W, Navarro R, Graser U, Petrov R, Weigelt G, Bresson Y, Hofmann KH, Beckman U, Henning T, Laun W, Leinert C, Kraus S, Robbe-Dubois S, Vakili F, Richichi A, Abraham P, Augereau J, Behrend J, Berio P, Berruyer N, Chesneau O, Clausse JM, Connot C, Demyk K, Danchi WC, Dugué M, Finger G, Flament S, Glazenberg A, Hannenburg H, Heining M, Hugues Y, Hron J, Jankov S, Kerschbaum F, Kroes G, Linz H, Lizon J, Mathias P, Mathar R, Matter A, Menut JL, Meisenheimer K, Millour F, Nardetto N, Neumann U, Nussbaum E, Niedzielski A, Mosoni L, Olofsson J, Rabbia Y, Ratzka T, Rigal F, Roussel A, Schertl D, Schmider F, Stecklum B, Thiebaut E, Vannier M, Valat B, Wagner K, Waters LBFM (2008) MATISSE: perspective of imaging in the mid-infrared at the VLTI. *SPIE* 7013:E70, DOI 10.1117/12.789412
- Ludwig HG (2006) Hydrodynamical simulations of convection-related stellar micro-variability. I. Statistical relations for photometric and photocentric variability. *A&A*445:661–671, DOI 10.1051/0004-6361:20042102, arXiv:astro-ph/0509441
- Malbet F, Perrin G (2007) Proceedings of the Euro Summer School "Observation and Data Reduction with the VLT Interferometer". *New Astronomy Review* 51:563–564, DOI 10.1016/j.newar.2007.06.001
- Malbet F, Lachaume R, Berger J, Colavita MM, di Folco E, Eisner JA, Lane BF, Millan-Gabet R, Ségransan D, Traub WA (2005) New insights on the AU-scale circumstellar structure of FU Orionis. *A&A*437:627, DOI 10.1051/0004-6361:20042556, arXiv:astro-ph/0503619
- Malbet F, Buscher D, Weigelt G, Garcia P, Gai M, Lorenzetti D, Surdej J, Hron J, Neuhäuser R, Kern P, Jocu L, Berger J, Absil O, Beckmann U, Corcione L, Duvert G, Filho M, Labeye P, Le Coarer E, Li Causi G, Lima J, Perraut K, Tatulli E, Thiébaud E, Young J, Zins G, Amorim A, Aringer B, Beckert T, Benisty M, Bonfils X, Cabral A, Chelli A, Chesneau O, Chiavassa A, Corradi R, De Becker M, Delboulbé A, Duchêne G, Forveille T, Haniff C, Herwats E, Hofmann K, Le Bouquin J, Ligor S, Loreggia D, Marconi A, Moitinho A, Nisini B, Petrucci P, Rebordao J, Speziali R, Testi L, Vitali F (2008) VSI: the VLTI spectro-imager. *SPIE* 7013:E68, DOI 10.1117/12.789710
- Malbet F, Cotton W, Duvert G, Lawson P, Chiavassa A, Young J, Baron F, Buscher D, Rengaswamy S, Kloppeborg B, Vannier M, Mugnier L (2010) The 2010 interferometric imaging beauty contest. In: *Society of Photo-Optical Instrumentation Engineers (SPIE) Conference Series*, Society of Photo-Optical Instrumentation Engineers (SPIE) Conference Series, vol 7734, DOI 10.1117/12.857066, 1007.4473
- Masset FS, Papaloizou JCB (2003) Runaway Migration and the Formation of Hot Jupiters. *ApJ*588:494–508, DOI 10.1086/373892, arXiv:astro-ph/0301171
- McAlister HA, ten Brummelaar TA, Gies DR, Huang W, Bagnuolo WG Jr, Shure MA, Sturmman J, Sturmman L, Turner NH, Taylor SF, Berger DH, Baines EK, Grundstrom E, Ogden C, Ridgway ST, van Belle G (2005) First Results from the CHARA Array. I. An Interferometric and Spectroscopic Study of the Fast Rotator α Leonis (Regulus). *ApJ*628:439–452, DOI 10.1086/430730, arXiv:astro-ph/0501261
- McCaughrean MJ, O'Dell CR (1996) Direct Imaging of Circumstellar Disks in the Orion Nebula.

- AJ111:1977, DOI 10.1086/117934
- Meimon S, Mugnier LM, Le Besnerais G (2005) Convex approximation to the likelihood criterion for aperture synthesis imaging. *Journal of the Optical Society of America A* 22:2348–2356, DOI 10.1364/JOSAA.22.002348
- Meimon S, Mugnier LM, Le Besnerais G (2008) Self-calibration approach for optical long-baseline interferometry imaging. *Journal of the Optical Society of America A* 26:108, DOI 10.1364/JOSAA.26.000108, 0812.1178
- Meisenheimer K, Tristram KRW, Jaffe W, Israel F, Neumayer N, Raban D, Röttgering H, Cotton WD, Graser U, Henning T, Leinert C, Lopez B, Perrin G, Prieto A (2007) Resolving the innermost parsec of Centaurus A at mid-infrared wavelengths. *A&A*471:453–465, DOI 10.1051/0004-6361:20066967, arXiv:0707.0177
- Meisner JA, Jaffe WJ, Le Poole RS, Pereira SF, Quirrenbach A, Raban D, Vosteen A (2010) The polarization-based collimated beam combiner and the proposed NOVA fringe tracker (NFT) for the VLTI. In: *Society of Photo-Optical Instrumentation Engineers (SPIE) Conference Series*, Society of Photo-Optical Instrumentation Engineers (SPIE) Conference Series, vol 7734, DOI 10.1117/12.858271
- Mennesson B, Perrin G, Chagnon G, du Coudé Foresto V, Ridgway S, Merand A, Salome P, Borde P, Cotton W, Morel S, Kervella P, Traub W, Lacasse M (2002) Evidence for Very Extended Gaseous Layers around O-rich Mira Variables and M Giants. *ApJ*579:446–454, DOI 10.1086/342671
- Millan-Gabet R, Monnier JD, Berger J, Traub WA, Schloerb FP, Pedretti E, Benisty M, Carleton NP, Hagenauer P, Kern P, Labeye P, Lacasse MG, Malbet F, Perraut K, Pearlman M, Thureau N (2006) Bright Localized Near-Infrared Emission at 1–4 AU in the AB Aurigae Disk Revealed by IOTA Closure Phases. *ApJ*645:L77–L80, DOI 10.1086/506153, arXiv:astro-ph/0606059
- Millan-Gabet R, Malbet F, Akeson R, Leinert C, Monnier J, Waters R (2007) The Circumstellar Environments of Young Stars at AU Scales. In: B Reipurth, D Jewitt, & K Keil (ed) *Protostars and Planets V*, pp 539–554
- Millour F, Chesneau O, Borges Fernandes M, Meilland A, Mars G, Benoist C, Thiébaud E, Stee P, Hofmann K, Baron F, Young J, Bendjoya P, Carciofi A, Domiciano de Souza A, Driebe T, Jankov S, Kervella P, Petrov RG, Robbe-Dubois S, Vakili F, Waters LBFM, Weigelt G (2009) A binary engine fuelling HD 87643's complex circumstellar environment. Determined using AMBER/VLTI imaging. *A&A*507:317–326, DOI 10.1051/0004-6361/200811592, 0908.0227
- Millour F, Meilland A, Chesneau O, Stee P, Kanaan S, Petrov R, Mourard D, Kraus S (2011) Imaging the spinning gas and dust in the disc around the supergiant A[e] star HD 62623. *A&A*526:A107, DOI 10.1051/0004-6361/201016193, 1012.2957
- Monnier JD (2003) Optical interferometry in astronomy. *Reports on Progress in Physics* 66:789–857, DOI 10.1088/0034-4885/66/5/203, arXiv:astro-ph/0307036
- Monnier JD (2007) Phases in interferometry. *New A Rev.*51:604–616, DOI 10.1016/j.newar.2007.06.006
- Monnier JD, Millan-Gabet R, Tuthill PG, Traub WA, Carleton NP, Coudé du Foresto V, Danchi WC, Lacasse MG, Morel S, Perrin G, Porro IL, Schloerb FP, Townes CH (2004) High-Resolution Imaging of Dust Shells by Using Keck Aperture Masking and the IOTA Interferometer. *ApJ*605:436–461, DOI 10.1086/382218, arXiv:astro-ph/0401363
- Monnier JD, Pedretti E, Thureau N, Berger JP, Millan-Gabet R, ten Brummelaar T, McAlister H, Sturmman J, Sturmman L, Muirhead P, Tannirkulam A, Webster S, Zhao M (2006) Michigan Infrared Combiner (MIRC): commissioning results at the CHARA Array. *SPIE* 6268:E55, DOI 10.1117/12.671982
- Monnier JD, Zhao M, Pedretti E, Thureau N, Ireland M, Muirhead P, Berger JP, Millan-Gabet R, Van Belle G, ten Brummelaar T, McAlister H, Ridgway S, Turner N, Sturmman L, Sturmman J, Berger D (2007) Imaging the Surface of Altair. *Science* 317:342–, DOI 10.1126/science.1143205, 0706.0867
- Mourard D, Clause JM, Marcotto A, Perraut K, Tallon-Bosc I, Bério P, Blazit A, Bonneau D, Bosio S, Bresson Y, Chesneau O, Delaa O, Hénault F, Hughes Y, Lagarde S, Merlin G, Roussel A, Spang A, Stee P, Tallon M, Antonelli P, Foy R, Kervella P, Petrov R, Thiébaud E, Vakili F, McAlister H, ten Brummelaar T, Sturmman J, Sturmman L, Turner N, Farrington C, Goldfinger PJ (2009) VEGA: Visible spectroGraph and polArimeter for the CHARA array: principle and performance. *A&A*508:1073–1083, DOI 10.1051/0004-6361/200913016
- Narayan R, Nityananda R (1986) Maximum entropy image restoration in astronomy. *ARA&A*24:127–170, DOI 10.1146/annurev.aa.24.090186.001015
- Nenkova M, Ivezić Ž, Elitzur M (2002) Dust Emission from Active Galactic Nuclei. *ApJ*570:L9–L12, DOI 10.1086/340857, astro-ph/0202405
- Nenkova M, Sirocky MM, Ivezić Ž, Elitzur M (2008a) AGN Dusty Tori. I. Handling of Clumpy Media. *ApJ*685:147–159, DOI 10.1086/590482, 0806.0511
- Nenkova M, Sirocky MM, Nikutta R, Ivezić Ž, Elitzur M (2008b) AGN Dusty Tori. II. Observational Implications of Clumpiness. *ApJ*685:160–180, DOI 10.1086/590483, 0806.0512
- Nordlund Å (1982) Numerical simulations of the solar granulation. I - Basic equations and methods.

- A&A107:1–10
- Ohnaka K (2004) Warm water vapor envelope in the supergiants α Ori and α Her and its effects on the apparent size from the near-infrared to the mid-infrared. *A&A*421:1149–1158, DOI 10.1051/0004-6361:20035668, arXiv:astro-ph/0406053
- Ohnaka K, Bergeat J, Driebe T, Graser U, Hofmann KH, Köhler R, Leinert C, Lopez B, Malbet F, Morel S, Paresce F, Perrin G, Preibisch T, Richichi A, Schertl D, Schöller M, Sol H, Weigelt G, Wittkowski M (2005) Mid-infrared interferometry of the Mira variable RR Sco with the VLTI MIDI instrument. *A&A*29:1057–1067, DOI 10.1051/0004-6361:20041052
- Ohnaka K, Driebe T, Hofmann KH, Weigelt G, Wittkowski M (2008) Spatially resolved dusty torus toward the red supergiant WOH G64 in the Large Magellanic Cloud. *A&A*484:371–379, DOI 10.1051/0004-6361:200809469, 0803.3823
- Ohnaka K, Hofmann K, Benisty M, Chelli A, Driebe T, Millour F, Petrov R, Schertl D, Stee P, Vakili F, Weigelt G (2009) Spatially resolving the inhomogeneous structure of the dynamical atmosphere of Betelgeuse with VLTI/AMBER. *A&A*503:183–195, DOI 10.1051/0004-6361/200912247, 0906.4792
- Olofsson J, Benisty M, Augereau JC, Pinte C, Ménard F, Tatulli E, Berger JP, Malbet F, Merin B, van Dishoeck EF, Lacour S, Pontoppidan KM, Monin JL, Brown JM, Blake GA (2011) Warm dust resolved in the cold disk around T Chamaeleontis with VLTI/AMBER. *A&A*528:L6, DOI 10.1051/0004-6361/201016074, 1102.4976
- Paladini C, Aringer B, Hron J, Nowotny W, Sacuto S, Höfner S (2009) Interferometric properties of pulsating C-rich AGB stars. Intensity profiles and uniform disc diameters of dynamic model atmospheres. *A&A*501:1073–1085, DOI 10.1051/0004-6361/200911938, 0904.2166
- Pauls TA, Young JS, Cotton WD, Monnier JD (2005) A Data Exchange Standard for Optical (Visible/IR) Interferometry. *PASP*117:1255–1262, DOI 10.1086/444523, arXiv:astro-ph/0508185
- Perrin G, Coudé du Foresto V, Ridgway ST, Mennesson B, Ruilier C, Mariotti JM, Traub WA, Lacasse MG (1999) Interferometric observations of R Leonis in the K band. First direct detection of the photospheric pulsation and study of the atmospheric intensity distribution. *A&A*345:221–232
- Perrin G, Ridgway ST, Coudé du Foresto V, Mennesson B, Traub WA, Lacasse MG (2004a) Interferometric observations of the supergiant stars α Orionis and α Herculis with FLUOR at IOTA. *A&A*418:675–685, DOI 10.1051/0004-6361:20040052, arXiv:astro-ph/0402099
- Perrin G, Ridgway ST, Mennesson B, Cotton WD, Woillez J, Verhoelst T, Schuller P, Coudé du Foresto V, Traub WA, Millan-Gabet R, Lacasse MG (2004b) Unveiling Mira stars behind the molecules. Confirmation of the molecular layer model with narrow band near-infrared interferometry. *A&A*426:279–296, DOI 10.1051/0004-6361:20041098
- Perrin G, Verhoelst T, Ridgway ST, Cami J, Nguyen QN, Chesneau O, Lopez B, Leinert C, Richichi A (2007) The molecular and dusty composition of Betelgeuse's inner circumstellar environment. *A&A*474:599–608, DOI 10.1051/0004-6361:20077863, 0709.0356
- Petrov RG, Malbet F, Weigelt G, Antonelli P, Beckmann U, Bresson Y, Chelli A, Dugué M, Duvert G, Gennari S, Glück L, Kern P, Lagarde S, Le Coarer E, Lisi F, Millour F, Perraut K, Puget P, Rantakyö F, Robbe-Dubois S, Roussel A, Salinari P, Tatulli E, Zins G, Accardo M, Acke B, Agabi K, Altariba E, Arezki B, Aristidi E, Baffa C, Behrend J, Blöcker T, Bonhomme S, Busoni S, Cassaing F, Clause JM, Colin J, Connot C, Delboulbé A, Domiciano de Souza A, Driebe T, Feautrier P, Ferruzzi D, Forveille T, Fossat E, Foy R, Fraix-Burnet D, Gallardo A, Giani E, Gil C, Glentzlin A, Heiden M, Heining M, Hernandez Utrera O, Hofmann KH, Kamm D, Kiekebusch M, Kraus S, Le Contel D, Le Contel JM, Lesourd T, Lopez B, Lopez M, Magnard Y, Marconi A, Mars G, Martinot-Lagarde G, Mathias P, Mège P, Monin JL, Mouillet D, Mourard D, Nussbaum E, Ohnaka K, Pacheco J, Perrier C, Rabbia Y, Rebattu S, Reynaud F, Richichi A, Robini A, Sacchetti M, Schertl D, Schöller M, Solscheid W, Spang A, Stee P, Stefanini P, Tallon M, Tallon-Bosc I, Tasso D, Testi L, Vakili F, von der Lühe O, Valtier JC, Vannier M, Ventura N (2007) AMBER, the near-infrared spectro-interferometric three-telescope VLTI instrument. *A&A*464:1–12, DOI 10.1051/0004-6361:20066496
- Quirrenbach A (2000) Phase Referencing. In: P R Lawson (ed) *Principles of Long Baseline Stellar Interferometry*, p 143
- Quirrenbach A, Buscher DF, Mozurkewich D, Hummel CA, Armstrong JT (1994) Maximum-entropy maps of the Be shell star zeta Tauri from optical long-baseline interferometry. *A&A*283:L13–L16
- Raban D, Jaffe W, Röttgering H, Meisenheimer K, Tristram KRW (2009) Resolving the obscuring torus in NGC 1068 with the power of infrared interferometry: revealing the inner funnel of dust. *MNRAS*394:1325–1337, DOI 10.1111/j.1365-2966.2009.14439.x, 0901.1306
- Readhead ACS, Nakajima TS, Pearson TJ, Neugebauer G, Oke JB, Sargent WLW (1988) Diffraction-limited imaging with ground-based optical telescopes. *AJ*95:1278–1296, DOI 10.1086/114724
- Renard S, Thiébaud E, Malbet F (2011) Image reconstruction in optical interferometry: Benchmarking the regularization. *A&A*1106.4508

- Robinson FJ, Demarque P, Li LH, Sofia S, Kim YC, Chan KL, Guenther DB (2004) Three-dimensional simulations of the upper radiation-convection transition layer in subgiant stars. *MNRAS* 347:1208–1216
- Roddi F (1986) Triple correlation as a phase closure technique. *Optics Communications* 60:145–148, DOI 10.1016/0030-4018(86)90168-9
- Ryde N, Lambert DL, Richter MJ, Lacy JH (2002) Detection of Water Vapor in the Photosphere of Arcturus. *ApJ* 580:447–458, DOI 10.1086/343040, arXiv:astro-ph/0207368
- Ryde N, Harper GM, Richter MJ, Greathouse TK, Lacy JH (2006) Water Vapor on Betelgeuse as Revealed by TEXES High-Resolution 12 μ m Spectra. *ApJ* 637:1040–1055, DOI 10.1086/498420, arXiv:astro-ph/0510177
- Sacuto S, Aringer B, Hron J, Nowotny W, Paladini C, Verhoelst T, Höfner S (2011) Observing and modeling the dynamic atmosphere of the low mass-loss C-star R Sculptoris at high angular resolution. *A&A* 525:A42, DOI 10.1051/0004-6361/200913786, 1010.1350
- Schmitt HR, Pauls TA, Tycner C, Armstrong JT, Zavala RT, Benson JA, Gilbreath GC, Hindsley RB, Hutter DJ, Johnston KJ, Jorgensen AM, Mozurkewich D (2009) Navy Prototype Optical Interferometer Imaging of Line Emission Regions of β Lyrae Using Differential Phase Referencing. *ApJ* 691:984–996, DOI 10.1088/0004-637X/691/2/984, 0801.4772
- Scholz M, Takeda Y (1987) Model study of wavelength-dependent limb-darkening and radii of M-type giants and supergiants. *A&A* 186:200–212
- Schwarzschild M (1975) On the scale of photospheric convection in red giants and supergiants. *ApJ* 195:137–144
- Sedlmayr E (1994) From Molecules to Grains. In: Jorgensen UG (ed) *IAU Colloq. 146: Molecules in the Stellar Environment*, Lecture Notes in Physics, Berlin Springer Verlag, vol 428, p 163, DOI 10.1007/3-540-57747-5-42
- Ségransan D (2007) Observability and UV coverage. *New Astronomy Review* 51:597–603, DOI 10.1016/j.newar.2007.06.005
- Siess L, Dufour E, Forestini M (2000) An internet server for pre-main sequence tracks of low- and intermediate-mass stars. *A&A* 358:593–599, arXiv:astro-ph/0003477
- Skilling J, Bryan RK (1984a) Maximum Entropy Image Reconstruction - General Algorithm. *MNRAS* 211:111
- Skilling J, Bryan RK (1984b) Maximum Entropy Image Reconstruction - General Algorithm. *MNRAS* 211:111
- Stothers R, Leung KC (1971) Luminosities, masses and periodicities of massive red supergiants. *A&A* 10:290–300
- ten Brummelaar TA, McAlister HA, Ridgway ST, Bagnuolo WG Jr, Turner NH, Sturmman L, Sturmman J, Berger DH, Oden CE, Cadman R, Hartkopf WI, Hopper CH, Shure MA (2005) First Results from the CHARA Array. II. A Description of the Instrument. *ApJ* 628:453–465, DOI 10.1086/430729, arXiv:astro-ph/0504082
- Thiébaud E (2008) MIRA: an effective imaging algorithm for optical interferometry. *SPIE* 7013:E43, DOI 10.1117/12.788822
- Thiebaut E, Giovannelli JF (2010) Image reconstruction in optical interferometry. *IEEE Signal Processing Magazine* 27:97–109, DOI 10.1109/MSP.2009.934870, 0909.2228
- Thompson AR, Moran JM, Swenson GW Jr (2001) *Interferometry and Synthesis in Radio Astronomy*, 2nd Edition
- Townes CH, Wishnow EH (2008) Interferometry at mid-infrared wavelengths: the ISI system. In: *Society of Photo-Optical Instrumentation Engineers (SPIE) Conference Series*, Society of Photo-Optical Instrumentation Engineers (SPIE) Conference Series, vol 7013, DOI 10.1117/12.791197
- Tristram KRW, Meisenheimer K, Jaffe W, Schartmann M, Rix HW, Leinert C, Morel S, Wittkowski M, Röttgering H, Perrin G, Lopez B, Raban D, Cotton WD, Graser U, Paresce F, Henning T (2007) Resolving the complex structure of the dust torus in the active nucleus of the Circinus galaxy. *A&A* 474:837–850, DOI 10.1051/0004-6361:20078369, arXiv:0709.0209
- Tsuji T (2000) Water in Emission in the Infrared Space Observatory Spectrum of the Early M Supergiant Star μ Cephei. *ApJ* 540:L99–L102, DOI 10.1086/312879, arXiv:astro-ph/0008058
- Tuthill PG, Monnier JD, Danchi WC (1999) A dusty pinwheel nebula around the massive star WR104. *Nature* 398:487–489, DOI 10.1038/19033, arXiv:astro-ph/9904092
- Tuthill PG, Monnier JD, Danchi WC, Hale DDS, Townes CH (2002) Imaging the Disk around the Luminous Young Star LkH α 101 with Infrared Interferometry. *ApJ* 577:826–838, DOI 10.1086/342235, arXiv:astro-ph/0206105
- Urry CM, Padovani P (1995) Unified Schemes for Radio-Loud Active Galactic Nuclei. *PASP* 107:803, DOI 10.1086/133630, arXiv:astro-ph/9506063
- Vakili F, Mourard D, Bonneau D, Morand F, Stee P (1997) Subtle structures in the wind of P Cygni.

- A&A323:183–188
- Varnière P, Quillen AC, Frank A (2004) The Evolution of Protoplanetary Disk Edges. *ApJ*612:1152–1162, DOI 10.1086/422542, arXiv:astro-ph/0306422
- Verhooft T, Decin L, van Malderen R, Hony S, Cami J, Eriksson K, Perrin G, Deroo P, Vandenbussche B, Waters LBFM (2006) Amorphous alumina in the extended atmosphere of α Orionis. *A&A*447:311–324, DOI 10.1051/0004-6361:20053359, arXiv:astro-ph/0510486
- Wedemeyer-Böhm S, Kamp I, Bruls J, Freytag B (2005) Carbon monoxide in the solar atmosphere. I. Numerical method and two-dimensional models. *A&A*438:1043–1057, DOI 10.1051/0004-6361:20042550
- Weigelt G (1991) Triple-Correlation Imaging in Optical Astronomy. *Progress in Optics* 29:293–319, DOI 10.1016/0030-4018(86)90168-9
- Weigelt G, Wittkowski M, Balega YY, Beckert T, Duschl WJ, Hofmann KH, Men'shchikov AB, Schertl D (2004) Diffraction-limited bispectrum speckle interferometry of the nuclear region of the Seyfert galaxy μ ASTROBJ_cNGC 1068 μ ASTROBJ_c in the H and K' bands. *A&A*425:77–87, DOI 10.1051/0004-6361:20040362
- Weiner J (2004) Mira's Apparent Size Variations due to a Surrounding Semiopaque H_2O Layer. *ApJ*611:L37–L40, DOI 10.1086/423672
- Wittkowski M, Kervella P, Arsenault R, Paresce F, Beckert T, Weigelt G (2004) VLTI/VINCI observations of the nucleus of NGC 1068 using the adaptive optics system MACAO. *A&A*418:L39–L42, DOI 10.1051/0004-6361:20040118, arXiv:astro-ph/0403497
- Wittkowski M, Boboltz DA, Ohnaka K, Driebe T, Scholz M (2007) The Mira variable S Orionis: relationships between the photosphere, molecular layer, dust shell, and SiO maser shell at 4 epochs. *A&A*470:191–210, DOI 10.1051/0004-6361:20077168, 0705.4614
- Wittkowski M, Boboltz DA, Driebe T, Le Bouquin JB, Millour F, Ohnaka K, Scholz M (2008) J, H, K spectro-interferometry of the Mira variable S Orionis. *A&A*479:L21–L24, DOI 10.1051/0004-6361:20079237, 0801.0594
- Woitke P, Helling C, Winters JM, Jeong KS (1999) On the formation of warm molecular layers. *A&A*348:L17–L20
- Wolf S (2008) Signatures of planets in young and evolved circumstellar disks. *Physica Scripta Volume T* 130(1):014,025, DOI 10.1088/0031-8949/2008/T130/014025
- Wolf S, D'Angelo G (2005) On the Observability of Giant Protoplanets in Circumstellar Disks. *ApJ*619:1114–1122, DOI 10.1086/426662, astro-ph/0410064
- Wolf S, Klahr H (2002) Large-Scale Vortices in Protoplanetary Disks: On the Observability of Possible Early Stages of Planet Formation. *ApJ*578:L79–L82, DOI 10.1086/344501, astro-ph/0209002
- Wolf S, Gueth F, Henning T, Kley W (2002) Detecting Planets in Protoplanetary Disks: A Prospective Study. *ApJ*566:L97–L99, DOI 10.1086/339544, astro-ph/0201197
- Wolf S, Moro-Martín A, D'Angelo G (2007) Signatures of planets in protoplanetary and debris disks. *Planet. Space Sci.*55:569–581, DOI 10.1016/j.pss.2006.04.035
- Wolf S, Malbet F, Alexander R, Berger JP, Creech-Eakman M, Duchene G, Dutrey A, Mordasini C, Pantin E, Pont F, Pott JU, Tatulli E, Testi L (2012) Circumstellar disks and planets. Science cases for next-generation optical/infrared long-baseline interferometers. *A&A Rev.*1203.6271
- Woodruff HC, Eberhardt M, Driebe T, Hofmann KH, Ohnaka K, Richichi A, Schertl D, Schöller M, Scholz M, Weigelt G, Wittkowski M, Wood PR (2004) Interferometric observations of the Mira star α Ceti with the VLTI/VINCI instrument in the near-infrared. *A&A*421:703–714, DOI 10.1051/0004-6361:20035826, arXiv:astro-ph/0404248
- Woodruff HC, Ireland MJ, Tuthill PG, Monnier JD, Bedding TR, Danchi WC, Scholz M, Townes CH, Wood PR (2009) The Keck Aperture Masking Experiment: Spectro-Interferometry of Three Mira Variables from 1.1 to 3.8 μ m. *ApJ*691:1328–1336, DOI 10.1088/0004-637X/691/2/1328, 0811.1642
- Young JS, Baldwin JE, Boysen RC, Haniiff CA, Lawson PR, Mackay CD, Pearson D, Rogers J, St-Jacques D, Warner PJ, Wilson DMA, Wilson RW (2000) New views of Betelgeuse: multi-wavelength surface imaging and implications for models of hotspot generation. *MNRAS*315:635–645
- Young JS, Badsen AG, Bharmal NA, Boysen RC, O'Donova B, Seneta EB, Thorsteinsson H, Thureau ND, Pedretti E, Monnier JD (2004) Unveiling Alpha Orionis. In: UK National Astronomy Meeting
- Zavala RT, Hummel CA, Boboltz DA, Ojha R, Shaffer DB, Tycner C, Richards MT, Hutter DJ (2010) The Algol Triple System Spatially Resolved at Optical Wavelengths. *ApJ*715:L44–L48, DOI 10.1088/2041-8205/715/1/L44, 1005.0626
- Zhao M, Gies D, Monnier JD, Thureau N, Pedretti E, Baron F, Merand A, ten Brummelaar T, McAlister H, Ridgway ST, Turner N, Sturmman J, Sturmman L, Farrington C, Goldfinger PJ (2008) First Resolved Images of the Eclipsing and Interacting Binary β Lyrae. *ApJ*684:L95–L98, DOI 10.1086/592146, 0808.0932
- Zhao M, Monnier JD, Pedretti E, Thureau N, Mérand A, Ten Brummelaar T, McAlister H, Ridgway ST,

Turner N, Sturmman J, Sturmman L, Goldfinger PJ, Farrington C (2009) Imaging and Modeling Rapidly Rotating Stars: α Cephei and α Ophiuchi. *ApJ*701:209–224, DOI 10.1088/0004-637X/701/1/209, 0906.2241

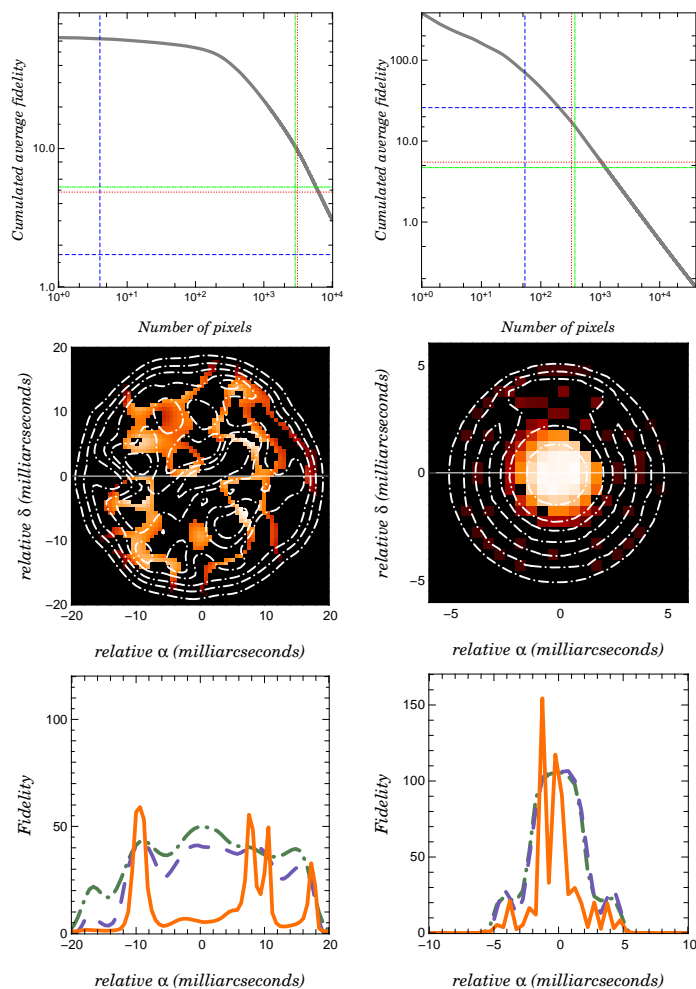


Fig. 10 **Top row:** cumulated average fidelity for the supergiant and evolved star cases. Blue dashed, green dashed-dotted, red dotted vertical lines: number of pixels with intensity greater than a given fraction of the total image intensity, respectively: $4 \cdot 10^{-4}$, $1 \cdot 10^{-4}$, $4 \cdot 10^{-5}$ for the supergiant (left), $5 \cdot 10^{-3}$, $1 \cdot 10^{-3}$, $5 \cdot 10^{-4}$ for the evolved star (right). Horizontal lines share the same color code: median fidelity for pixels having intensity greater than a given fraction of image total intensity. **Central row:** original model image filtered with a fidelity threshold (supergiant: 10, evolved star: 10). **Bottom row:** fidelity profile along the solid cut line in central row. Orange solid line: fidelity; green dashed-dotted line: model image; dashed blue: reconstructed image. Units are given in fidelity, image profiles have been scaled to fit the figure.

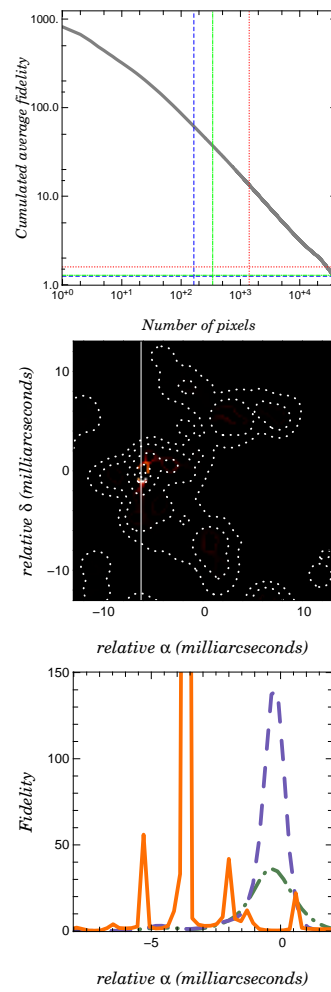


Fig. 11 Top: cumulated average fidelity for the AGN case. Blue dashed, green dashed-dotted, red dotted vertical lines: number of pixels with intensity greater than a given fraction of the total image intensity i.e. $1 \cdot 10^{-3}$, $5 \cdot 10^{-4}$, $1 \cdot 10^{-4}$. Horizontal lines share the same color code: median fidelity for pixels having intensity greater than a given fraction of image total intensity. **Central:** original model image filtered with a fidelity threshold (AGN: 3). **Bottom:** fidelity profile along the solid cut line in central row. Orange solid line: fidelity; green dashed-dotted line: model image; dashed blue: reconstructed image. Units are given in fidelity, image profiles have been scaled to fit the figure.